

Observation of spiciness interannual variability in the Pacific pycnocline

Nicolas Kolodziejczyk¹ and Fabienne Gaillard¹

Received 14 July 2012; revised 25 October 2012; accepted 25 October 2012; published 13 December 2012.

[1] Monthly gridded fields predominantly based on global Argo in situ temperature and salinity data are used to analyze the density-compensated anomaly of salinity (spiciness anomaly) in the pycnocline of the subtropical and tropical Pacific Ocean between 2004 and 2011. Interannual variability in the formation, propagation and fate of spiciness anomalies are investigated. The spiciness anomalies propagate on the isopycnal surface $\sigma_\theta = 25.5$ along the subtropical-tropical pycnocline advected by the mean currents. They reach the Pacific Western Tropics in about 5–6 years in the Southern Hemisphere and about 7–8 years in the Northern Hemisphere. Their amplitude strongly diminishes along the way and only very weak spiciness anomalies seem to reach the equator in the Western Tropics. A complex-EOF analysis of interannual salinity anomalies on $\sigma_\theta = 25.5$ highlights two dominant modes of variability at interannual scale: i) the former shows a variability of 5–7 years predominant in the Northern Hemisphere, and ii) the latter displays an interannual variability of 2 to 3 years more marked in the Southern Hemisphere. The significant correlation of this second mode with ENSO index suggests that spiciness formation in the southeastern Pacific (SEP) is affected by ENSO tropical interannual variability. A diagnosis of the mechanisms governing the interannual generation of spiciness in the SEP region leads the authors to suggest that the spiciness interannual variability in the sub-surface is linked to the equatorward migration of the isopycnal outcrop line $\sigma_\theta = 25.5$ into the area of maximum salinity. Quantitative analysis based on Turner angle reveals the dominance of the spiciness injection mechanism occurring through convective mixing at the base of mixed layer.

Citation: Kolodziejczyk, N., and F. Gaillard (2012), Observation of spiciness interannual variability in the Pacific pycnocline, *J. Geophys. Res.*, 117, C12018, doi:10.1029/2012JC008365.

1. Introduction

[2] To a first-order approximation, a spiciness anomaly along a constant potential density surface (by reference to the surface pressure) is a linear combination of temperature and salinity anomalies weighted by thermal contraction and haline expansion coefficients respectively, on condition that the spatial and temporal variations of both coefficients are small [Tailleux *et al.*, 2005]. Given that temperature and salinity anomalies are compensated on a given isopycnal surface, observing spiciness comes to observing temperature- or salinity-anomalies on a constant isopycnal surface. Spiciness anomalies have thus to the first order, neither density nor

pressure signature. So, they are advected like a passive tracer in the thermocline mean circulation from the subtropical eastern region, where they are generated from the surface mixed layer (ML), toward the western boundary in the tropics or directly into the equatorial band [e.g., Lazar *et al.*, 2001; Yeager and Large, 2004; Luo *et al.*, 2005; Laurian *et al.*, 2006; Nonaka and Sasaki, 2007; Doney *et al.*, 2007].

[3] The generation and propagation of salinity (or temperature) anomalies on potential density surfaces from the subtropical to tropical regions have recently been investigated in numerous model studies [e.g., Lazar *et al.*, 2001, 2002; Schneider, 2000; Yeager and Large, 2004, 2007; Luo *et al.*, 2005; Laurian *et al.*, 2006; Nonaka and Sasaki, 2007; Doney *et al.*, 2007; Laurian *et al.*, 2009]. Finding observational evidence is more difficult [Sasaki *et al.*, 2010; Ren and Riser, 2010]. The basin-wide network of expendable bathythermograph (XBT) data has allowed the tracking of temperature anomalies subducted from the subtropics to tropics at decadal time scale [Schneider *et al.*, 1999; Zhang and Liu, 1999; Luo and Yamagata, 2001], but the lack of associated salinity measurements in these studies has not allowed to separate spiciness anomalies on a constant isopycnal surface

¹IFREMER, Laboratoire de Physique des Océans, UMR 6523, CNRS/Ifremer/IRD/UBO, Plouzané, France.

Corresponding author: N. Kolodziejczyk, IFREMER, Laboratoire de Physique des Océans, UMR 6523, CNRS/Ifremer/IRD/UBO, F-29280, Plouzané, France. (nicolas.kolodziejczyk@gmail.com)

©2012. American Geophysical Union. All Rights Reserved.
0148-0227/12/2012JC008365

from the temperature anomalies induced by the vertical displacement of the isopycnals associated with high baroclinic modes of Rossby waves within the pycnocline [Liu and Shin, 1999; Liu, 1999].

[4] The unprecedented effort made in the deployment of Argo floats since the early 2000s has allowed the first in situ observations of the basin-wide temperature and salinity from the surface down to a depth of 2 000 m with a vertical, horizontal and temporal resolution well-suited to a good tracking and description of spiciness. From Argo measurements, Sasaki *et al.* [2010] provided the first evidence of propagation, within the pycnocline, of a negative spiciness anomaly advected by the mean currents across the northern Pacific Ocean between 2001 and 2008.

[5] In the Pacific Ocean, the compensated water masses formation region is mainly the eastern subtropical zone (hereafter, northeastern Pacific and southeastern Pacific are denoted as NEP and SEP, respectively). In these regions, spiciness anomalies are generated via surface and sub-surface processes. These regions are characterized by compensating horizontal gradients of Sea Surface Temperature (SST) and Sea Surface Salinity (SSS) that induce a low Sea Surface Density (SSD) gradient allowing a large meridional displacement of the outcropping isopycnals during the winter season due to the winter loss of buoyancy. In his work in the maximum SSS area, Kessler [1999] could not link the downstream salinity variability on $\sigma_\theta = 24.5$ with surface SST and SSS. However, Nonaka and Sasaki [2007] provided evidence on a mechanism of subduction of spiciness anomalies (on the deeper $\sigma_\theta = 25.3$) through simulations of the SST and SSS meridional gradients located further south in the SEP. In this region, they found that the spiciness anomaly subduction is correlated to the meridional displacement of the outcropping isopycnal across the SST and SSS gradients: the excess of surface buoyancy loss in winter can force the outcrop line to migrate anomalously equatorward in warmer SST and saltier SSS. It thus induces subduction of warmer and saltier anomalies from the surface to the internal thermocline along a given isopycnal. Laurian *et al.* [2009] explained spiciness subduction in the northeastern subtropical Atlantic by the same mechanism.

[6] On the other hand, from Argo float measurements, Yeager and Large [2007] proposed that the vertical mixing at the base of the mixed layer was responsible for the injection of spiciness. In the spiciness formation regions of SEP between 15°S and 35°S, a weak stratification in winter coincides with a large and destabilizing vertical salinity gradient, favored by higher salinity at the surface than at the pycnocline depth in the area of maximum SSS in the subtropics [Yeager and Large, 2004, 2007; Luo *et al.*, 2005]. The destabilization of the buoyancy profile in the winter mixed layer leads to both convective boundary layer mixing and generation of a strongly density-compensated layer at the base of the mixed layer within the pycnocline. These authors computed the vertical Turner angle (Tu) [Ruddick, 1983; You, 2002] so as to quantify the degree of density compensation of the T-S gradients of an upper-ocean water column and to identify spiciness injection during the late winter of each hemisphere. Although both processes have been associated with the formation of spiciness anomalies in the

southern subtropical mixed layer [Luo *et al.*, 2005], the complete characterization as well as the interannual variability of spiciness generation and the links with atmospheric and oceanic variability are still open issues that will be addressed in this study.

[7] In the western tropical Pacific Ocean, the fate of spiciness anomalies ventilated in the interior pycnocline is also a key issue to be addressed for gaining more insight into the subtropical pycnocline remote connections with other regions. According to ventilated thermocline theory [Luyten *et al.*, 1983; Liu, 1994], the thermohaline properties advected by the mean circulation either reach the equatorial region by following a direct interior pathway from subtropics to the tropics [Johnson and McPhaden, 1999] and via western boundary currents [Luo and Yamagata, 2001; Capotondi *et al.*, 2005; Luo *et al.*, 2005], or recirculate poleward in the western boundary currents [Zhang and Liu, 1999] as shown in the North Atlantic Ocean by Laurian *et al.* [2006].

[8] The following feedback mechanism between subtropical and tropical regions was proposed by Gu and Philander [1997]: the thermocline bridge ventilates heat anomalies subducted from the subtropics into the equatorial band and impacts the equatorial SST; then, the tropical and extratropical winds are in turn affected and feedback the influx in subtropics. Using a simple model these authors demonstrated that these processes can lead to decadal to inter-decadal oscillations. In OGCM model studies of the Pacific Ocean, Schneider [2000, 2004] qualitatively showed the existence of such a feed-back generated by spiciness anomalies artificially injected in the western tropical Pacific. Although, an artificial fresh (salty) spiciness anomaly introduced in the equatorial band amplifies (weakens) the amplitude of ENSO, the subtropical-tropical spiciness feed-back remains weak in this model and enhances only a slight decadal modulation of the tropical variability.

[9] Indeed, some studies reveal that spiciness anomalies are probably strongly attenuated along their path toward the equator both in the Northern Hemisphere (between $\sigma_\theta = 25$ – 25.5 kg.m^{-3}) [Sasaki *et al.*, 2010] and in the Southern Hemisphere for the South Pacific Eastern Subtropical Mode Water (SPESMW; $\sigma_\theta = 24.5$ – 25.8 kg.m^{-3}) [Sato and Suga, 2009]. There, the vertical compensation of salinity and temperature produces enhanced double diffusive mixing that strongly erodes, the SPESMW anomalies of temperature and salinity after the austral winter. The same mechanism was noted by Johnson [2006] who observed a strong erosion of highly compensated winter subducted water during the following seasons for two individual Argo floats measurements located in the SEP.

[10] In this study, interannual variability in the formation, propagation and fate of spiciness anomalies in the subtropical and tropical pycnocline of the Pacific Ocean are investigated by using a sufficiently dense set of temperature-salinity profiles from Argo floats, moorings measurements and CTD. Section 2 of this paper introduces the data and analysis method. The interannual variability of spiciness anomaly propagation within the Pacific thermocline in both hemispheres is addressed in section 3. Section 4 describes the characteristics and interannual variability of spiciness anomaly formation in the SEP

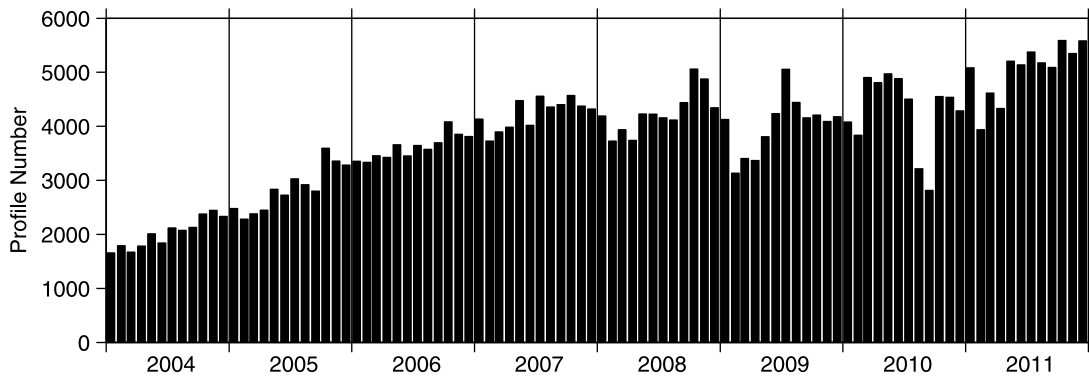


Figure 1. Number of profiles used for each monthly optimal interpolation in the Pacific Ocean between 120°E–80°W and 40°S–50°N, over the period 2004–2011.

generation zone. At last, a synthesis and discussion of the main results of the study are proposed.

2. Data and Method

[11] This study uses monthly gridded fields of temperature and salinity obtained with ISAS (In Situ Analysis System), an optimal estimation tool designed for the synthesis of the Argo global data set [Gaillard *et al.*, 2009]. Although Argo (<http://www.argo.net>) started in 2000–2001 in the Northern Hemisphere, the subtropical and tropical Pacific is reasonably sampled only since 2004. We thus decided to focus our study on the 2004–2011 period. The gridded fields were produced over the global ocean by the ARIVO project with data sets downloaded from the Coriolis data center. The major contribution comes from the Argo array of profiling floats, from nearly 1500 profiles per month in 2004 to more than 5000 profiles per month in 2011 (Figure 1). This data subset is backed up by the TAO array of moorings in the tropical band. A few CTDs transmitted in real time are used but XBTs and X-CTDs were excluded from the analysis because of uncertainties in the fall rate. A climatological test was applied to the data set, and followed with a visual control of suspicious profiles. The temperature and salinity fields are reconstructed on 152 levels ranging from 0 to 2000 m depth, on a half degrees horizontal grid. This particular ARIVO analysis, called D2CA1S2 differs from the product used by von Schuckmann *et al.* [2009] on two respects: the reference climatology and the time period. While von Schuckmann *et al.* [2009] used WOA05 [Antonov *et al.*, 2006; Locarnini *et al.*, 2006] reference climatology, we use the average of von Schuckmann *et al.* [2009] on the period 2002–2008 named ARV09.

[12] For the purpose of spiciness analysis, the ARIVO monthly fields in z -coordinates was re-interpolated in sigma coordinates with $\Delta\sigma_\theta = 0.01 \text{ kg.m}^{-3}$ (Figure 2). Then, the monthly mean climatology of salinity on isopycnal surfaces was computed to remove the seasonal cycle and to produce interannual anomalies of salinity on a isopycnal surface. Thus, the variability of salinity due to vertical motion of isopycnal surface is removed, and only density-compensated anomalies are considered. The ARIVO product is estimated on a vertical grid with spacing of 10 m in the pycnocline that allow the vertical resolution of anomalies. Note that the salinity anomalies were computed on isopycnal surfaces only within the

extreme equatorward outcrop of the isopycnal surface between 2004 and 2011. Thus, only the interior salinity anomalies are considered, i.e., they are not in contact with the surface.

[13] In this study, the mean Montgomery potential and geostrophic velocities on isopycnal surfaces were computed following McDougall and Klocker [2010] (with use of GSW V2.0 library). The reference level for mean geostrophic velocities between 2004 and 2011 is the surface dynamic topography MDT_CNES-CLS09 based on GRACE (Gravity Recovery and Climate Experiment), satellite altimetry and in situ measurement [Rio *et al.*, 2011] combined with AVISO Sea Level Anomalies (SLA) [Ducet *et al.*, 2000] for the period 2004–2011. Encouragingly, in the subtropical-tropical Pacific Ocean, we obtain the same geostrophic velocities using the reference level of surface dynamic topography from Maximenko *et al.* [2009] as done by Sasaki *et al.* [2010], or using the MDT_CNES-CLS09 product.

[14] The statistical description of the interannual salinity patterns on a given isopycnal surface and of the mixed layer depth is performed with Complex Empirical Orthogonal Functions (C-EOFs). The C-EOFs algorithm ([Barnett, 1983]; routine from <http://hydr.ct.tudelft.nl/wbk/public/hooimeijer>) makes an EOF analysis on a Hilbert-transformed time-space series of data. Whereas classical EOF analysis captures only stationary patterns, C-EOF analysis finds co-varying patterns, which are phase-lagged in time and space, and catches them in a same propagating pattern.

[15] The buoyancy change due to temperature and salinity is expressed as follows:

$$\Delta B = -g \frac{\Delta\rho}{\rho_0} = g\alpha\Delta T - g\beta\Delta S \quad (1)$$

where $\rho_0 = 1026 \text{ kg.m}^{-3}$ is an ocean reference density, g is the gravitational acceleration, α and β are the coefficients of expansion for temperature and salinity, respectively. In regions of large vertical inversion of salinity (e.g., the region of sub-tropical SSS maxima), the stratifying effect of ΔT is significantly counteracted by the destabilizing salinity ΔS , which leads to a weakly stable buoyancy profile. When the effects by the destabilizing salinity profile and by the stabilizing temperature profile are opposed and equal in absolute value, they are compensated in density. Moreover, when the stabilizing effect of temperature profile is less than the destabilizing effect of salinity profile, the buoyancy profile

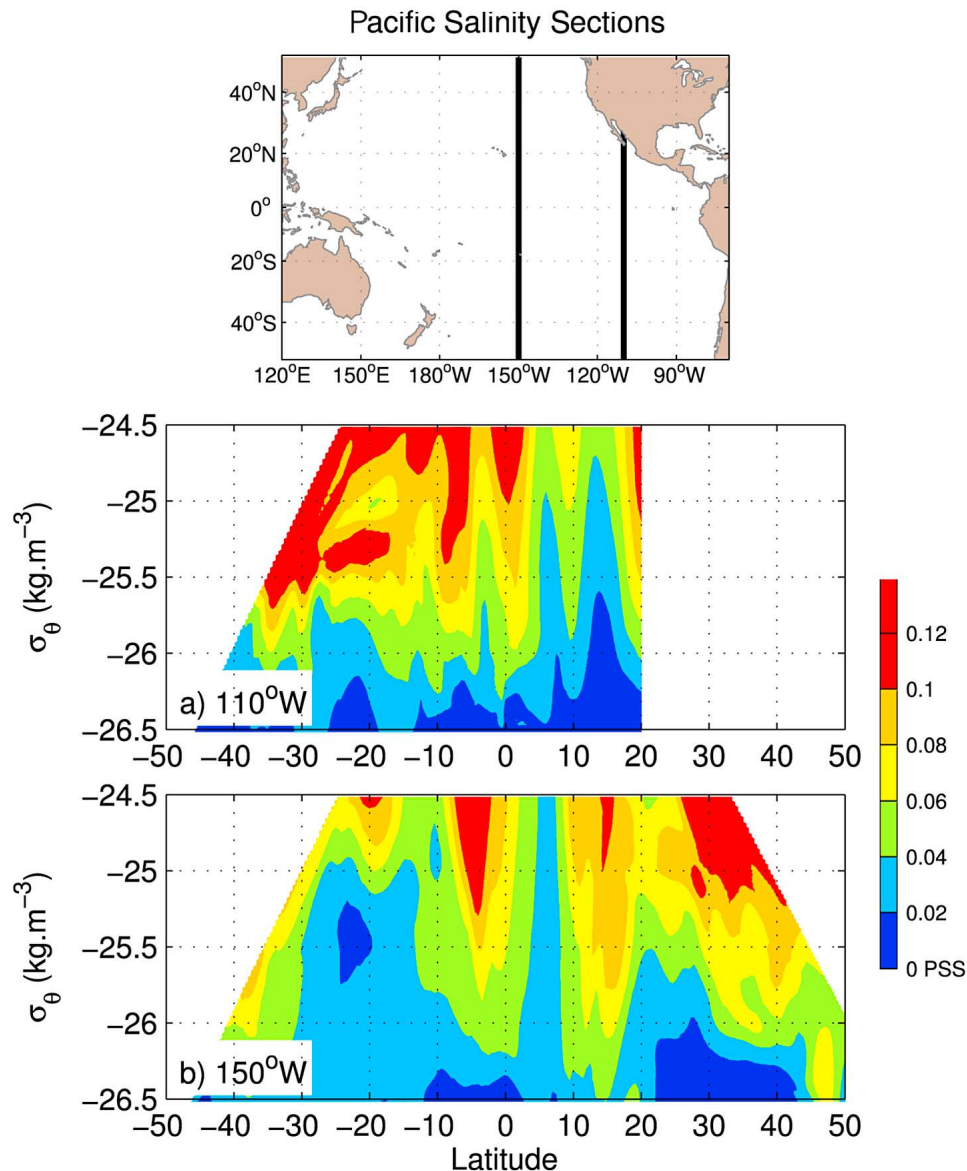


Figure 2. STD of isopycnal interannual salinity anomaly (in PSS; shaded) along the section (a) at 110°W between 50°S–20°N and (b) at 150°W between 50°N–50°N and $\sigma_\theta = 24$ –26.5 m depth from ARIVO/D2CA1S2 analysis between 2004 and 2011. Position of the 110°W and 150°W sections in the Pacific Ocean is shown in the topmost panel.

is gravitationally unstable, and thus generates convection and vertical mixing. In this study the degree of density compensation of vertical T and S gradients is quantified by the Turner angle [Ruddick, 1983; Yeager and Large, 2007]:

$$Tu = \text{atan}\left(\frac{\alpha\partial_z T + \beta\partial_z S}{\alpha\partial_z T - \beta\partial_z S}\right) \quad (2)$$

Under conditions of stabilized water column (i.e., $\partial_z T > 0$ and $\partial_z S < 0$), the Turner angle (Tu) is within $\pm 45^\circ$, when a destabilizing salinity gradient is concomitant with a stabilizing temperature gradient, $Tu > 45^\circ$. If $Tu > 71.6^\circ$ the process of double-diffusion starts to be active [Johnson, 2006], when Tu tends to 90° the buoyancy effects of $\partial_z T > 0$ and $\partial_z S > 0$ are of opposite sign and we are close to the

perfect density compensation [see Yeager and Large, 2004, 2007; Johnson, 2006].

3. Spiciness Propagation

3.1. Mean State and Interannual Variability

[16] In order to identify the density range where the strongest subsurface salinity anomalies are observed, we estimated the interannual variability of salinity anomalies by computing the standard deviation (STD) of monthly fields relative to the mean annual cycle of salinity on the isopycnals. A subsurface maximum is detected within the pycnocline. In the Southern Hemisphere between 35°S and 5°S, anomalies up to 0.1 PSS are observed in the range $\sigma_\theta = 25.0$ –26.0 $\text{kg}\cdot\text{m}^{-3}$ along 110°W (Figure 2a). In the Northern

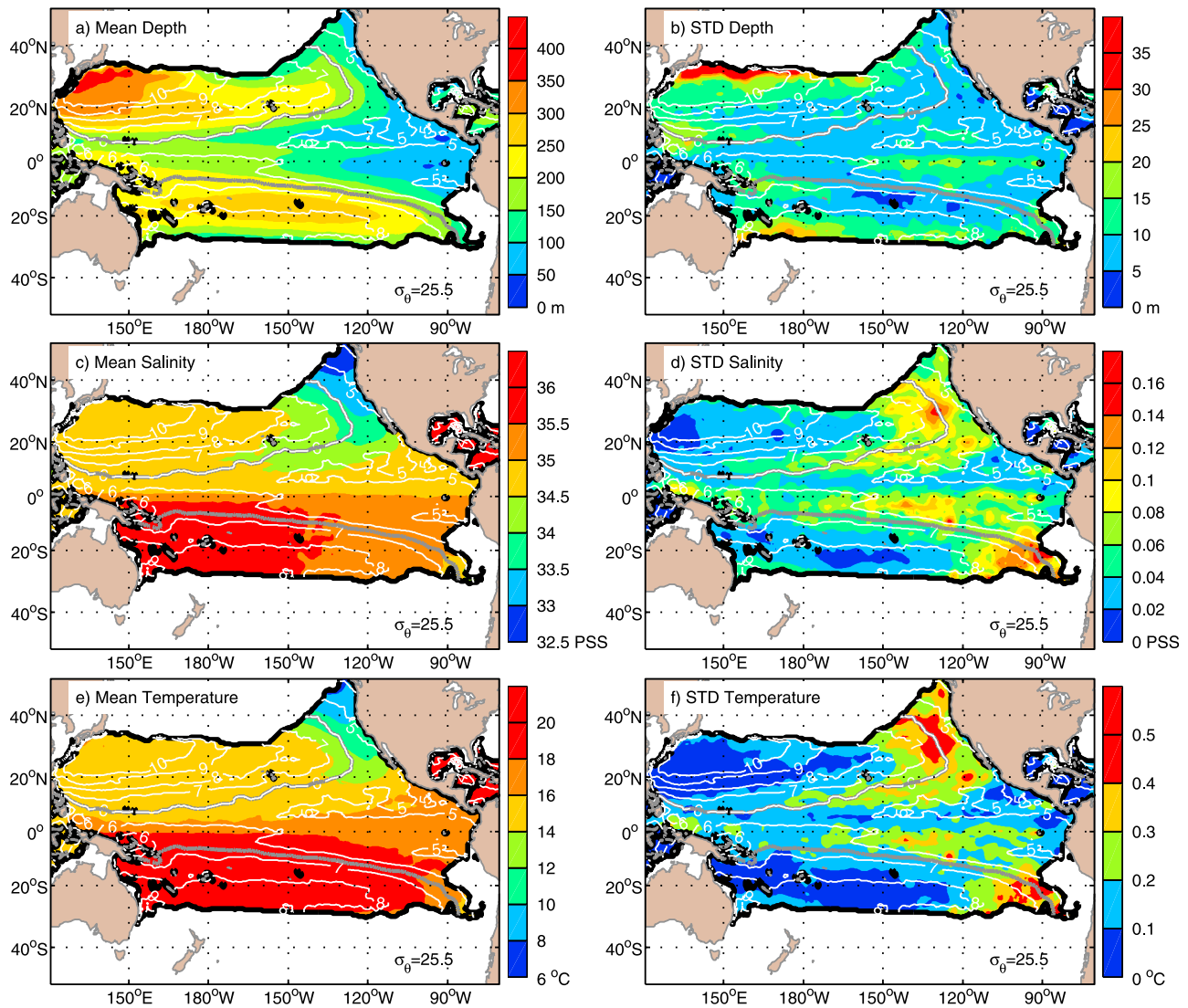


Figure 3. (a) Mean and (b) interannual STD of salinity (in PSS); (c) mean and (d) interannual STD of temperature (in $^{\circ}\text{C}$) and (e) mean and (f) interannual STD of depth (in m) on the isopycnal surface $\sigma_{\theta} = 25.5$ between 2004 and 2011. The thin white lines indicate the mean Montgomery potential isopleth (in $\text{m}^2 \text{s}^{-2}$) computed on the $\sigma_{\theta} = 25.5$ surface, and thick gray lines materialize the $6 \text{ m}^2 \text{s}^{-2}$ isopleth in the Northern Hemisphere and the $6.5 \text{ m}^2 \text{s}^{-2}$ isopleth in the Southern Hemisphere. The thick black contours show the most equatorward position of the outcrop position of $\sigma_{\theta} = 25.5$ surface during the same period.

Hemisphere between 10°N and 20°N (Figure 2b), strong salinity anomalies are also visible in subsurface (up to 0.1 PSS) with a maximum in the isopycnal range $\sigma_{\theta} = 24.5\text{--}26.0 \text{ kg.m}^{-3}$ along 150°W .

[17] In both hemispheres, the subtropical gyre is characterized by an anticyclonic circulation as shown by the mean 2004–2011 stream function (mean Montgomery isopleths) shown as white and gray contours in Figure 3. This circulation is associated with the deepening of the $\sigma_{\theta} = 25.5$ surface from less than 100 m in the eastern tropical Pacific and along the eastern boundary to more than 250 m depth in the southwestern hemisphere and to 350 m in the northwestern Pacific (Figure 3a). Between 8°N – 13°N , a band of shallow depth (less than 150 m) from west to east characterizes the mean position of the North Equatorial Counter Current (NECC). Along the equator, we note also a band of low depth

associated with the Equatorial Undercurrent (EUC). In the Pacific pycnocline, the meridional distribution of mean salinity and temperature show comparable structures (Figures 3c and 3e). The mean salinity and temperature on the $\sigma_{\theta} = 25.5$ are lower in the Northern Hemisphere (a mean difference of 2°C and 1 PSS). In both hemispheres, we note also a strong east-west contrast (greater than 2 PSS in the NEP) with lower values of temperature and salinity in the eastern regions.

[18] The variability of salinity and temperature represented by the interannual STD on $\sigma_{\theta} = 25.5$ is the highest in the SEP and NEP, with values of ± 0.12 PSS and 0.5°C (Figures 3d and 3f). Two tongues of higher salinity (temperature) variability are observed in both hemispheres with decreasing amplitude from NEP and SEP toward the western tropical Pacific; their distributions are similar along the gyre circulation. A large variability in the depth of the isopycnal (Figure 3b) is observed

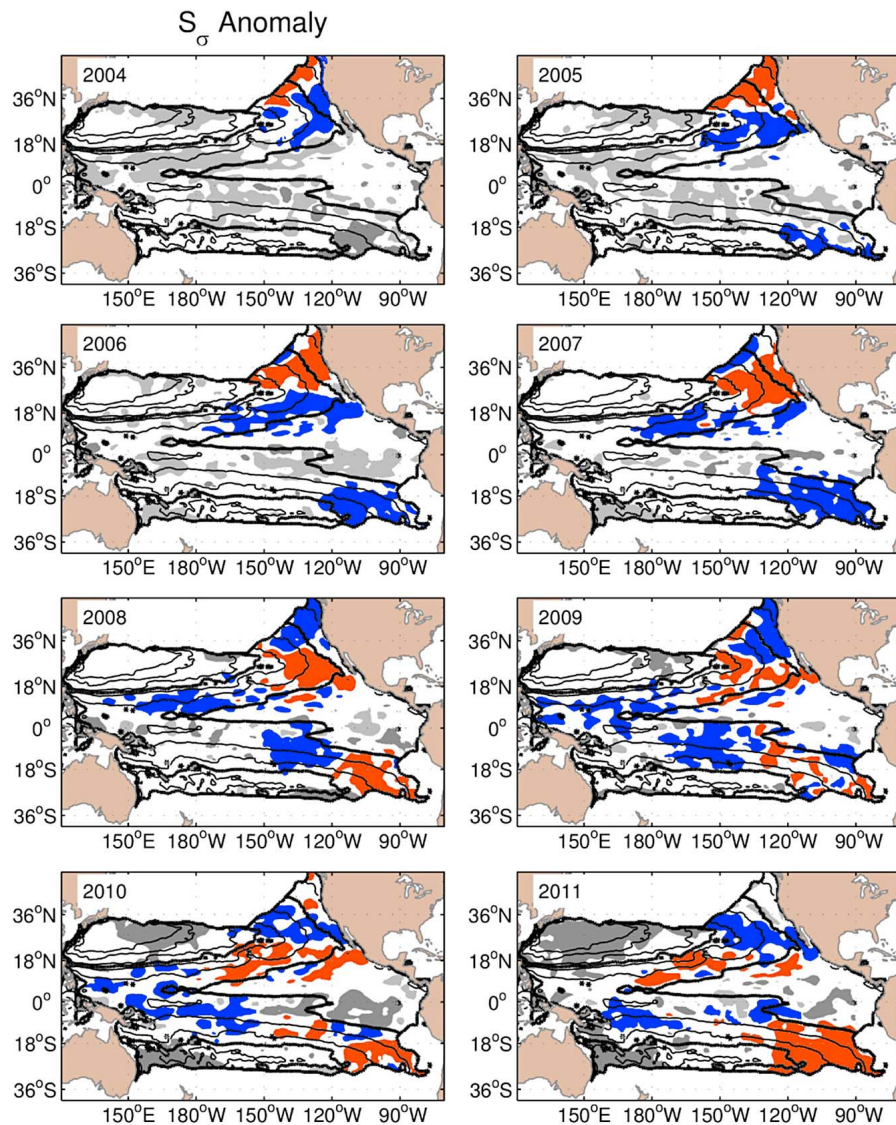


Figure 4. Mean annual isopycnal negative (dark gray) and positive (light gray) salinity anomalies greater than 0.03 PSS on the isopycnal surface $\sigma_{\theta} = 25.5$. For clarity, the positive and negative salinity anomalies described in the text have been colored in red and blue, respectively. The thick black streamlines show up the 5.5 and 8 $\text{m}^2 \text{s}^{-2}$ isopleths.

in 4 areas: i) in the northwestern Pacific near the Kuroshio current, ii) along the northern and southern $\sigma_{\theta} = 25.5$ outcrop line, iii) in the eastern equatorial band and iv) near the western tropical boundary at 10°S and 10°N (up to ± 15 m). It is worth noting that the regions with higher salinity and temperature variations correspond to the region where the depth variability of $\sigma_{\theta} = 25.5$ is the lowest except in the eastern equatorial band and along the outcrop line in the SEP (Figures 3b, 3d and 3f).

3.2. Salinity Anomalies

[19] The interannual variability of salinity on $\sigma_{\theta} = 25.5$ is associated in both hemispheres with the propagation of salinity anomalies along the gyre stream functions. In order to show the robustness of such propagating salinity anomalies, the mean annual salinity anomalies greater than 0.3 PSS in absolute value are plotted for each of the 8 years of available data (Figure 4; the anomalies of interest are color

shaded in blue and red for negative and positive anomalies, respectively). In the Northern Hemisphere, the negative salinity anomaly already reported by *Sasaki et al.* [2010] is visible in 2004 in the northeastern Pacific region (blue; Figure 4). It propagated along the streamline up to the western tropical region between 2004 and 2009. Then a positive salinity anomaly appears in 2004 in the subtropical NEP and propagates toward the western tropics until 2011, while a second negative salinity anomaly is generated in 2006 in the NEP region and propagates until 2011.

[20] In the SEP, a negative salinity anomaly appears during 2005–2006, then propagates along streamlines, and reaches the western tropics in 2011 (blue patch; Figure 4). A weak positive salinity anomaly is observed in 2008 then propagates to the middle South Pacific in 2010. During 2009 and 2010, a second weak negative anomaly is visible in the

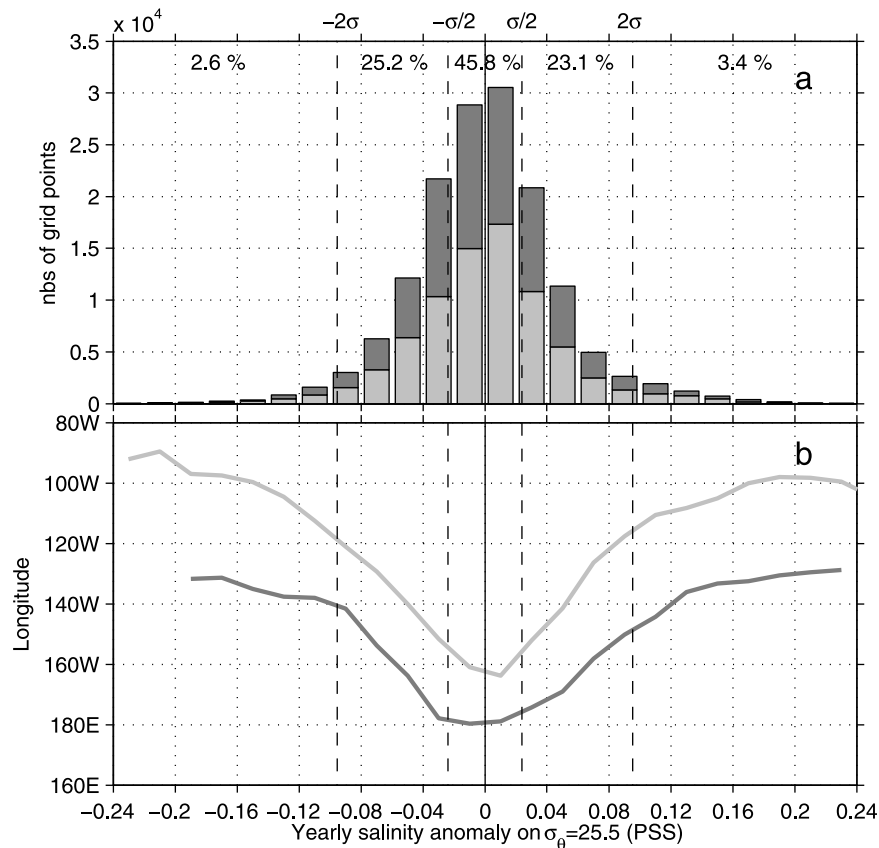


Figure 5. (a) Distribution of mean annual salinity interannual anomalies located within the the 5.5 and $8 \text{ m}^2 \text{ s}^{-2}$ isopleths in the Northern Hemisphere (dark gray) and in the Southern Hemisphere (light gray). The dashed lines correspond to two STD and half STD. (b) Mean longitude associated with each salinity anomalies class in the Northern Hemisphere (dark gray) and in the Southern Hemisphere (light gray).

SEP, preceding a second strong positive anomaly generated in 2010–2011.

[21] In total over the 8 years period, three salinity anomalies propagated from northeastern Pacific subtropics to the western tropical Pacific and four salinity anomalies from the southeastern Pacific subtropics. The salinity anomalies take about 7–8 years to travel across the basin in the North Pacific, and only 5–6 years the South Pacific. It can be explained by the longer path along the subtropical gyre in the Northern Hemisphere.

[22] In the Southern Hemisphere, it is worth noticing that the positive salinity anomaly observed in 2008 in the SEP decreases rapidly, becoming lower than 0.03 PSS before it reaches the central southern Pacific. In contrast, the negative anomalies are more robust in both Hemispheres. There is also some indication suggesting that negative salinity anomalies could reach the western equator. For instance in 2010–2011 negative anomalies are observed in the equatorial band, mostly in the south, consecutively to the arrival of negative salinity anomalies coming from both the Southern and Northern Hemisphere (Figure 4).

[23] In order to characterize the population of salinities anomalies, we plotted the distribution of yearly salinity anomalies by amplitude classes (Figure 5a) and the mean longitude for each class of salinity anomalies (Figure 5b). Only the grid points located between 5.5 and $8 \text{ m}^2 \text{ s}^{-2}$ isopleth (thick black streamlines in Figure 4) were taken into

account. The mean salinity anomaly is about null and the standard deviation is $\sigma = 0.048$ PSS. The distribution of salinity anomalies is slightly non-normal since only 94% of the basin-wide anomalies have an amplitude between two standard deviation (95% for normal distribution). The distribution shows that the very high values of salinity anomaly (greater than two standard deviation; $2\sigma = 0.096$ PSS) correspond to few grid points (about 6.0% of the total). These anomalies are mainly located east of 150°W in the Northern Hemisphere and east of 130°W in the Southern Hemisphere (Figure 5b), corresponding to the area of generation of salinity anomalies in the eastern subtropics. A large number of grid points (48.3% of the total) show moderate salinity anomalies (between $2\sigma = 0.096$ and $\sigma/2 = 0.024$ PSS). These points are mainly located between 150°W and 180°E in the Northern Hemisphere and between 120°W and 170°W in the Southern Hemisphere (Figure 5b), i.e., along the propagation path of the salinity anomalies. A closer look at Figure 5a reveals a slightly more positive than negative anomalies in the area of formation (3.4% versus 2.6% of the total), and oppositely slightly more negative than positive anomalies in the propagation area (25.2% versus 23.1% of the total). It suggests that during their propagation, the positive anomalies are slightly less robust than the negative anomalies, but the time series is still too short and the number of events still too low to make a robust statement.

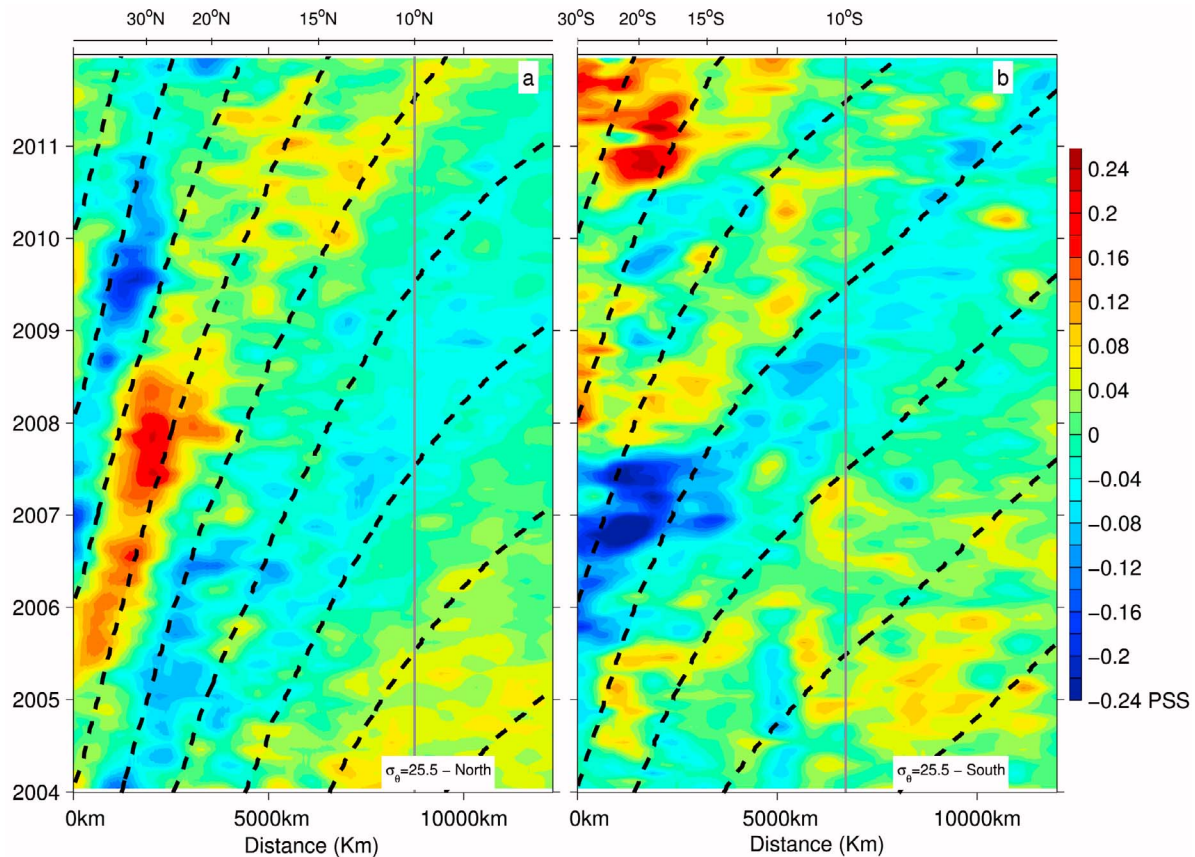


Figure 6. Distance-time diagram of salinity anomaly (in PSS) in the Northern Hemisphere (a) on $\sigma_\theta = 25.5$ surface along the $6 \text{ m}^2 \cdot \text{s}^{-2}$ mean Montgomery function isopleth (see Figure 2), and in the Southern Hemisphere (b) on $\sigma_\theta = 25.5$ surface along the $6.5 \text{ m}^2 \cdot \text{s}^{-2}$ mean Montgomery function isopleth (see Figure 2). The distance is counted from the most equatorward outcrop position of the $\sigma_\theta = 25.5$ in the NEP and SEP zones, toward the western boundary. Dashed black curves are the characteristics of the mean velocity along the given isopleth. The vertical gray line materialize the 10°N and 10°S latitude.

3.3. Propagation Velocity

[24] In order to quantify the velocity at which salinity anomalies propagate, the distance-time diagrams of salinity anomalies on $\sigma_\theta = 25.5$ were plotted along the $6 \text{ m}^2 \cdot \text{s}^{-2}$ isopleth in the Northern Hemisphere, and along the $6.5 \text{ m}^2 \cdot \text{s}^{-2}$ isopleth in the Southern Hemisphere (Figure 6). In the Northern Hemisphere (Figure 6a), the salinity anomalies show speeds of propagation toward the western tropics accelerating from 0.01 to $0.12 \text{ m} \cdot \text{s}^{-1}$, in good agreement with the mean current velocities (dashed black curves). A close examination of Figure 6a clearly shows, in the Northern Hemisphere, successive negative and positive patterns of salinity anomalies following the mean Montgomery isopleths contour toward the southwest. This distribution suggests a propagation of spiciness anomalies along the mean streamline. In the the Southern Hemisphere (Figure 6b), between 0 km and 4000 km , the salinity anomalies that originate from the southeastern Pacific seems rather stationary. Then, after 4000 km along the streamline, they propagate with a speed consistent with mean current velocity (at about $0.12 \text{ m} \cdot \text{s}^{-1}$). In this diagram we recognize the salinity anomalies previously described (section 3.2 and Figure 4).

[25] The 0 km origin is the extreme northward position occupied by outcropping line $\sigma_\theta = 25.5$ between 2004 and 2011. Since the maximum of spiciness anomalies appears at a distance of 500 km away from the outcrop in a layer which is never in contact with the surface, it suggests the interior generation of spiciness. The stationarity of anomalies in the first 4000 km might thus be explained by the interior generative process of injection during the late austral winter [Yeager and Large, 2007] that produces a sudden rise of saline anomalies as for example during austral winters 2007 and 2010.

3.4. Interannual Variability

[26] In order to infer the space-time scales associated with the dominant propagating patterns, a C-EOF decomposition was applied to the interannual anomaly of salinity on the $\sigma_\theta = 25.5$ surface and over the whole Pacific Ocean. The two leading modes explain a significant part (45.8%) of the salinity variance between 2004 and 2011, the first mode accounting for 32.2% (Figure 7a), and the second mode for 13.6% (Figure 7b). The two leading modes are intensified in the eastern subtropics, with maximum amplitude of 0.12 PSS

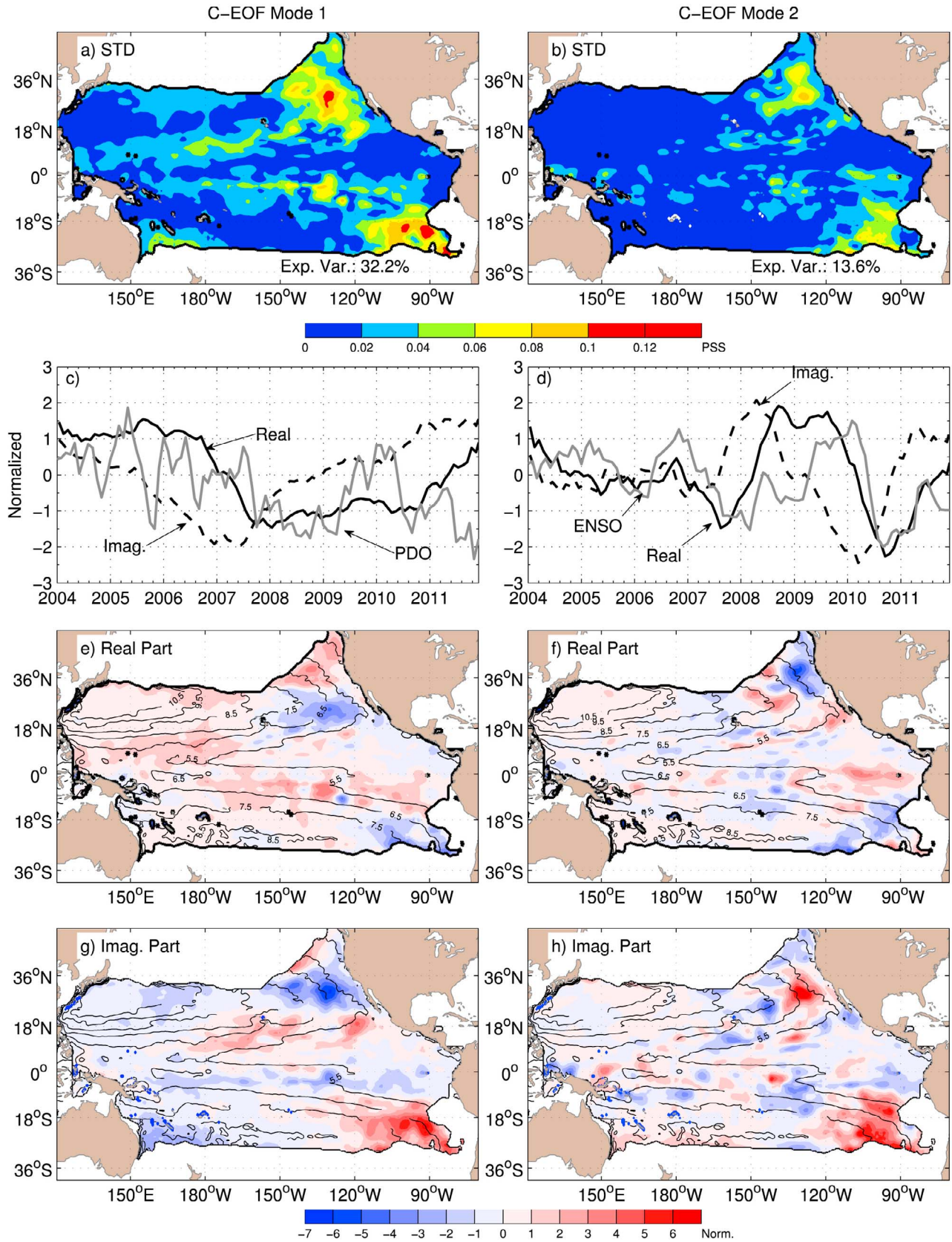


Figure 7

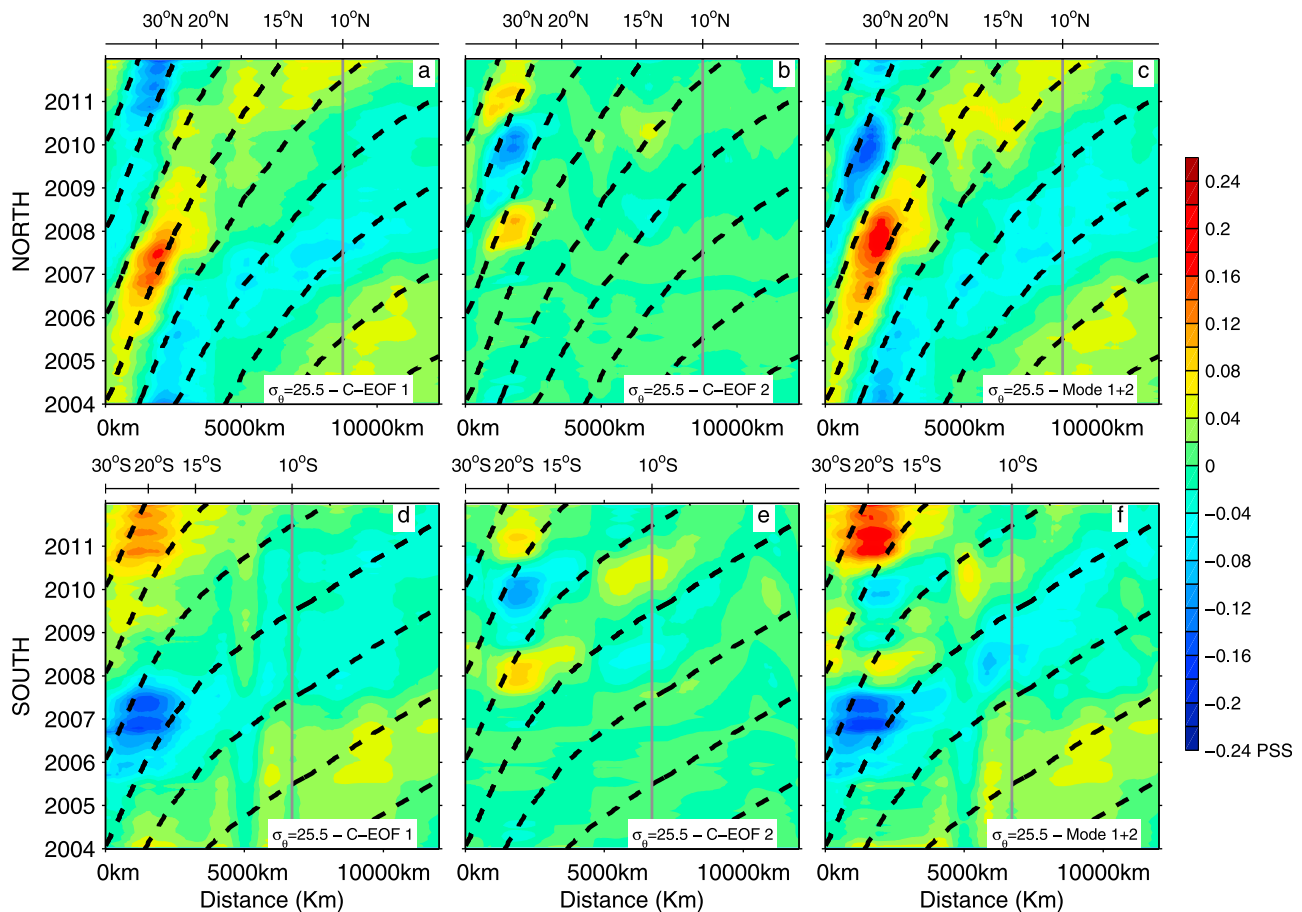


Figure 8. Distance-time diagram of salinity anomaly (in PSS) reconstructed using the (a) first, (b) second and (c) both C-EOF modes of salinity anomalies in the Northern Hemisphere, on $\sigma_\theta = 25.5$ surface along the $6 \text{ m}^2 \cdot \text{s}^{-2}$ mean Montgomery function isopleth (see Figure 2). (d) First, (e) second and (f) sum of both C-EOF patterns of salinity anomaly (in PSS) in the Southern Hemisphere on $\sigma_\theta = 25.5$ surface along the $6.5 \text{ m}^2 \cdot \text{s}^{-2}$ mean Montgomery function isopleth (see Figure 2). The distance is counted from the most equatorward outcrop position of the $\sigma_\theta = 25.5$ in the NEP and SEP zones, toward the western boundary. Dashed black curves are the characteristics of the mean velocity along the given isopleth. The vertical gray line materialize the 10°N and 10°S latitude.

(Figure 7a) for the first one, and more than 0.6 PSS for the second mode (Figure 7b). A C-EOF analysis performed separately in each hemisphere produces spacio-temporal patterns similar with the present analysis (not shown). The two-hemisphere C-EOFs are preferred since they better represent the basin-wide spatial covariances. The two leading C-EOF modes are sufficient to reconstruct most of the spiciness signal in the generation and propagation areas (compare Figures 6 and 8).

[27] The first mode captures a low frequency variability of about 5–7 years as seen in the time series of the principal component (Figure 7c). Given the spatial structure of the

modes, this variability is mostly expressed in the NEP, but also in the SEP generation zone (Figure 7a). The time series of the principal component of the real and imaginary parts of the second mode (Figure 7d) indicate a higher frequency (2–3 years) mainly found in the SEP and the eastern equatorial band (Figure 7b). Furthermore, the time series of the principal component of the second mode tracks well the ENSO index curve (Figure 7d; gray curve); it peaks positively in 2006–2007 and 2009–2010 and negatively in 2007–2008 and 2010–2011 (correlations: [$c_{\text{real}} = 0.56$; $\text{lag}_{\text{real}} = -4$ month; $c_{95\%} = 0.45$] and [$c_{\text{imag}} = -0.71$; $\text{lag}_{\text{imag}} = 4$ months; $c_{95\%} = 0.69$]). This finding suggests that the

Figure 7. C-EOF decomposition. STD of the interannual salinity anomalies (in PSS) on $\sigma_\theta = 25.5$ surface associated with the (a) first and (b) second C-EOF modes; normalized time series of the principal components of the real (solid) and the imaginary (dashed) parts of the C-EOF coefficients between 2004 and 2011 for the (c) first and (d) second modes. The gray curves are the PDO index and the ENSO index between 2004 and 2011. Normalized Spatial distributions of the amplitudes of the real and imaginary parts of (e and g) first and (f and h) second modes are shaded. The thin black contours are the mean Montgomery function isopleths (in $\text{m}^2 \cdot \text{s}^{-2}$), and the thick black contour indicates the extreme equatorward position of the outcrop position of the $\sigma_\theta = 25.0$ surface during the period 2004–2011.

generation of salinity anomalies on $\sigma_\theta = 25.5$ in the SEP is related to the tropical ENSO variability.

[28] The strongest variance of the first mode is located between 15°N and 40°N, eastward of 150°W in the sub-tropical NEP, and between 15°S and 40°S, eastward of 120°W in the sub-tropical SEP (Figure 7a). One should note that, at 30°S, the salinity anomalies are 180° out of phase with those at 30°N in the Northern Hemisphere: a negative anomaly is propagating from the SEP region toward the western tropical Pacific between 2006 and 2007 and 2010 and is followed by two positive anomalies, one between 2008 and 2010, and another starting in 2010 (Figures 7c, 7e and 7g). In the NEP, the emergence of a positive salinity anomaly at 40°N is concomitant with the positive phase of PDO index (Figures 7c and 7g) time series (between 2004 and 2007), while a negative anomaly of salinity appears in the SEP. In contrast, a negative (positive) salinity anomaly is formed in the NEP (SEP) when the PDO index is negative (2007–2011).

[29] The second C-EOF mode (Figures 7b, 7d, 7f and 7h) captures a strong variability of the salinity anomaly mainly in the eastern equator and in the SEP region. The alternating signs with decreasing amplitude along the streamlines of the C-EOF patterns (Figures 7d and 7f) also suggests the propagation and attenuation of the salinity anomalies toward the western tropics along the mean stream functions.

3.5. C-EOF Mode Propagation Velocity

[30] In order to assess in more details the propagation characteristics of each mode, the distance-time diagrams of salinity anomalies were plotted on $\sigma_\theta = 25.5$ along the $6 \text{ m}^2 \cdot \text{s}^{-2}$ isopleth in the Northern Hemisphere and along the $6.5 \text{ m}^2 \cdot \text{s}^{-2}$ isopleth in the Southern Hemisphere, as done for the total spiciness signal in Figure 6. In the Northern Hemisphere, the first dominant mode of C-EOF (Figure 8a) captures the long-term variability of propagating salinity anomalies and reveals speeds of propagation toward the western tropics accelerating from 0.01 to 0.12 $\text{m} \cdot \text{s}^{-1}$, which are in good agreement with the mean current velocities. In contrast, as seen previously, the second C-EOF mode fails to show a coherent spiciness propagation (Figure 8b). The major pattern of the reconstructed signal is thus explained by the first mode (Figure 8c).

[31] In the southern Pacific, the first C-EOF mode (Figure 8d) shows a negative anomaly starting from 2004 and propagating up to 5°S with velocities of about 0.10 $\text{m} \cdot \text{s}^{-1}$ comparable to the mean velocities (black dashed curves). Subsequently, a positive anomaly starts to develop in 2008 in the SEP. North of 15°S, the salinity anomalies are lagged with the anomalies located south of 15°S, but there is some inconsistency between their propagation and the mean velocities. In contrast with the Northern Hemisphere, the second mode expresses propagating salinity anomalies with comparable amplitudes and a higher frequency of generation, that both strongly modulate the variability of the reconstructed signal (Figures 8d–8f). In this study, as done for the Northern Hemisphere thermocline, the propagation velocities in the Southern Hemisphere were estimated to be accelerating from 0.01 to 0.11 $\text{m} \cdot \text{s}^{-1}$, from the subtropics to tropics, respectively, in agreement with the mean current speed.

[32] Although the salinity anomalies on $\sigma_\theta = 25.5$ propagate toward the equator at comparable speeds in both hemispheres, the salinity anomalies strongly weaken before they

reach the western tropical Pacific. Furthermore, our analysis highlighted two frequencies of generation: i) a ‘low’ frequency variability with a 5- to 7-year time-scale dominant in the Northern Hemisphere, and ii) a 2- to 3-year time-scale that modulates the Southern Hemisphere signal. It is worth recalling that the tracking of the ENSO index by the second C-EOF mode of variability suggests a link between both spiciness formation in the Southern Hemisphere and inter-annual variability between 30°N–20°S and ENSO atmospheric and/or oceanic dynamics. On the other hand, the first mode of C-EOF, which is dominant in the Northern Hemisphere, may be associated with a lower generation frequency likely ruled by PDO climate variability [Schneider, 2004; Kilpatrick et al., 2011].

4. Generation of Spiciness in the Southeastern Pacific

4.1. Processes of Generation

[33] Following Nonaka and Sasaki [2007] and Laurian et al. [2009], the formation of spiciness anomaly can be related to SST and SSS distributions via the late winter (in September) equatorward position of the isopycnal outcrop of the thermocline. The ample seasonal equatorward displacement of the outcrop lines is made possible by the weakness of the meridional Sea Surface Density (SSD) gradient. In Figure 9, the $\sigma_\theta = 25.5$ outcrop exhibits the largest meridional displacements during the austral late winters 2007 (magenta contour) and 2010 (blue contour). Within 35–30°S (90°W–70°W), the northward (westward) migration of the pycnocline outcrop lines allows the $\sigma_\theta = 25.5$ to be in contact with saltier and warmer (not shown) surface water masses from the area of maximum of SSS.

[34] The map of standard deviation of the interannual salinity anomalies on $\sigma_\theta = 25.5$ plotted in Figure 10 (see also Figure 3d) details the maxima of salinity anomaly (>0.12 PSS contoured in black in Figure 10) during 2004–2011. The maximum STD is composed of three local maxima: the first local maximum (up to 0.16 PSS) is centered on 20°S–90°W, the second (up to 0.13 PSS) on 24°S–100°W, and the third (up to 0.13 PSS) is located between 95°W and 80°W on 30°S. While the two first zones have been suggested by previous simulations [Yeager and Large, 2004], the later has never been reported before. These maxima are all located north-westward of the extreme equatorward outcrop line. If the salinity anomalies resulted from subduction, they would appear at the position of the late winter outcrop line. Since the bulk of the spiciness anomaly is located away from this line (gray contours), we favor the hypothesis of interior injection of spiciness.

[35] In order to quantify the dominance of either mechanisms of generation of salinity anomalies on $\sigma_\theta = 25.5$ (named late winter subduction versus interior injection), we have computed the late winter generation of salinity anomalies in the SEP as the difference between October and August salinity anomaly on $\sigma_\theta = 25.5$ (Figure 11). The late winters of 2007 and 2010, and in a lesser extent those of 2004 and 2011, exhibit the strongest increase of salinity, suggesting a clear relationship between the extreme equatorward late winter outcrop position and salinity involved in the generation process of spiciness. However, as previously noted in the propagation diagrams (Figure 6b), the two major salinity anomalies observed in 2007

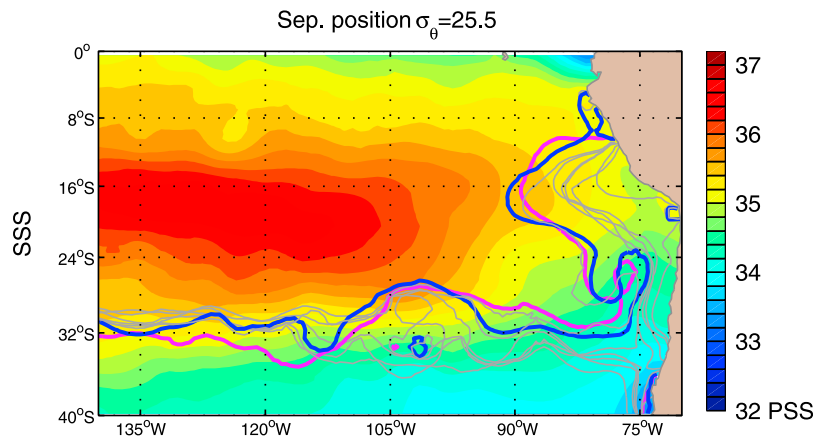


Figure 9. Mean September SSS in the SEP and September outcrop position of the isopycnal $\sigma_\theta = 25.5$ in September 2007 (magenta contour) and 2010 (blue contour), and in September 2004, 2005, 2006, 2008, 2009 and 2011 (gray contours).

and 2010, do not emanate exactly from the outcrop positions of $\sigma_\theta = 25.5$, but several hundreds of kilometers northward of the extreme equatorward position of this line. This is confirmed in Figure 11 where we observe that a significant part of the salinity anomalies are generated north of the outcrop position, suggesting a subsurface injection of spiciness in the interior pycnocline.

[36] In the SEP, the increase of salinity between August and October occurs on subducted isopycnals that are positioned just below the base of the mixed layer and which are therefore slightly denser than the sea surface density. Figure 12 represents the density of grid points as a function of $\sigma_\theta = 25.5$ -SSD distance (abscissa) and of the late winter spiciness generation

(ordinate) for points located in the region of maximum salinity contoured in black line in Figure 10. The abscissa corresponds to the difference between the $25.5 \text{ kg}\cdot\text{m}^{-3}$ and the SSD, i.e., the grid points located in the positive half plane lay below the base of the mixed layer during the winter. The ordinate corresponds to the October–August difference of salinity anomalies on $\sigma_\theta = 25.5$, i.e., grid point located in the positive (negative) half plane are associated with creation of positive (negative) anomaly of spiciness. In the upper-right hand positive half plane, the highest density of grid points is located away from the ordinate (Figure 12) associated with September SSD $0.1\text{--}0.2 \text{ kg}\cdot\text{m}^{-3}$ lower than the $\sigma_\theta = 25.5$ isopycnal density. It confirms that the highest increase of late

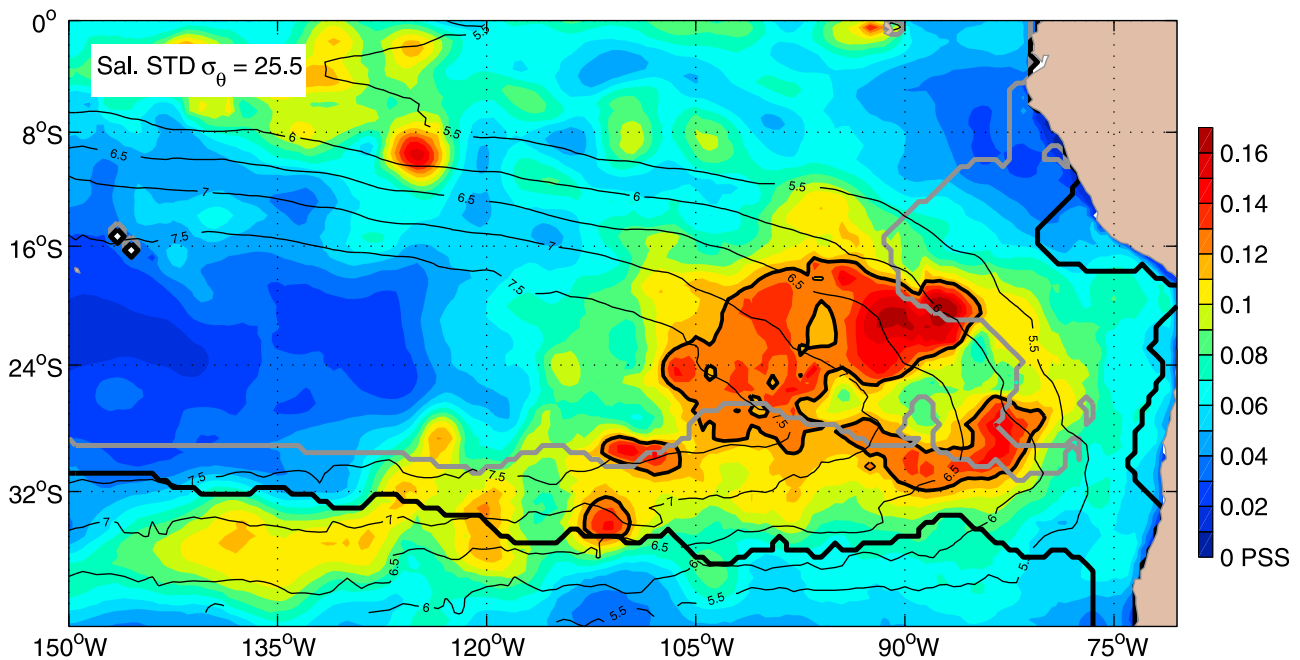


Figure 10. Standard deviation of the interannual salinity anomalies in the SEP. STD greater than 0.12 PSS are contoured in black. The thick gray line indicates the most equatorward outcrop position of $\sigma_\theta = 25.5$ between 2004 and 2011. The thick black line indicates the mean September outcrop position of $\sigma_\theta = 25.5$ between 2004 and 2011. The thin black lines indicate the mean Montgomery potential isopleth (in $\text{m}^2 \text{ s}^{-2}$) computed on the $\sigma_\theta = 25.5$ surface.

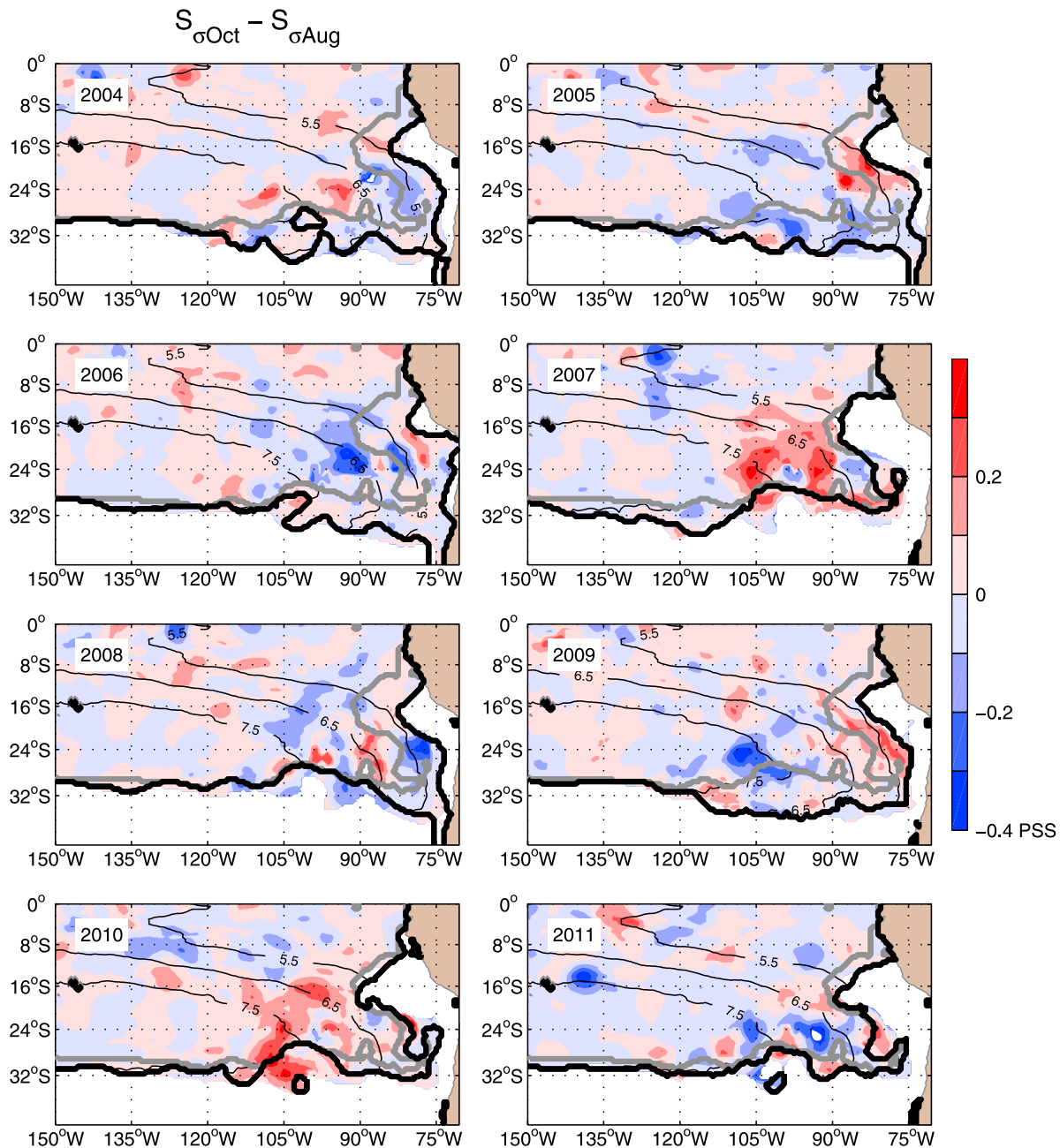


Figure 11. Late winter salinity generation (PSS) defined as the difference between October and August $\sigma_{\theta} = 25.5$ isopycnal interannual salinity anomalies for each year between 2004 and 2011 in the SEP. The thick gray line indicates the most equatorward outcrop position between 2004 and 2011. The thick black line indicates the September outcrop position during corresponding years indicated in each sub-figure.

winter salinity takes place below the surface mixed layer. That means that positive anomaly injection on the $\sigma_{\theta} = 25.5$ has occurred during winter mixing while the $\sigma_{\theta} = 25.5$ persists throughout the winter. It is mainly the case during the years 2007 and 2010 (red and green circle and cross; Figure 12) when strong positive anomaly rises in the SEP, as deduced from previous analysis. The negative salinity changes in late winter have in general lower amplitude than the positive changes, but are more densely distributed in the area between 0 to -0.1 PSS and 0.1 to 0.4 kg.m^{-3} . They occur when the September stratification between $\sigma_{\theta} = 25.5$ and

surface density remains large, probably advected from more poleward fresher latitudes. It is mainly the case during the years 2006, 2005 and 2009 (Figure 12) when negative anomaly rises in the SEP. Therefore, in the SEP, the late winter subduction fails to explain the bulk of subsurface formation of the strongest positive salinity anomalies between 35°S and 15°S . The same statement was made by *Yeager and Large* [2004] from numerical simulation studies. It drove them to propose that sub-surface injection of salinity is achieved through convective mixing at the base of the mixed layer in late winter.

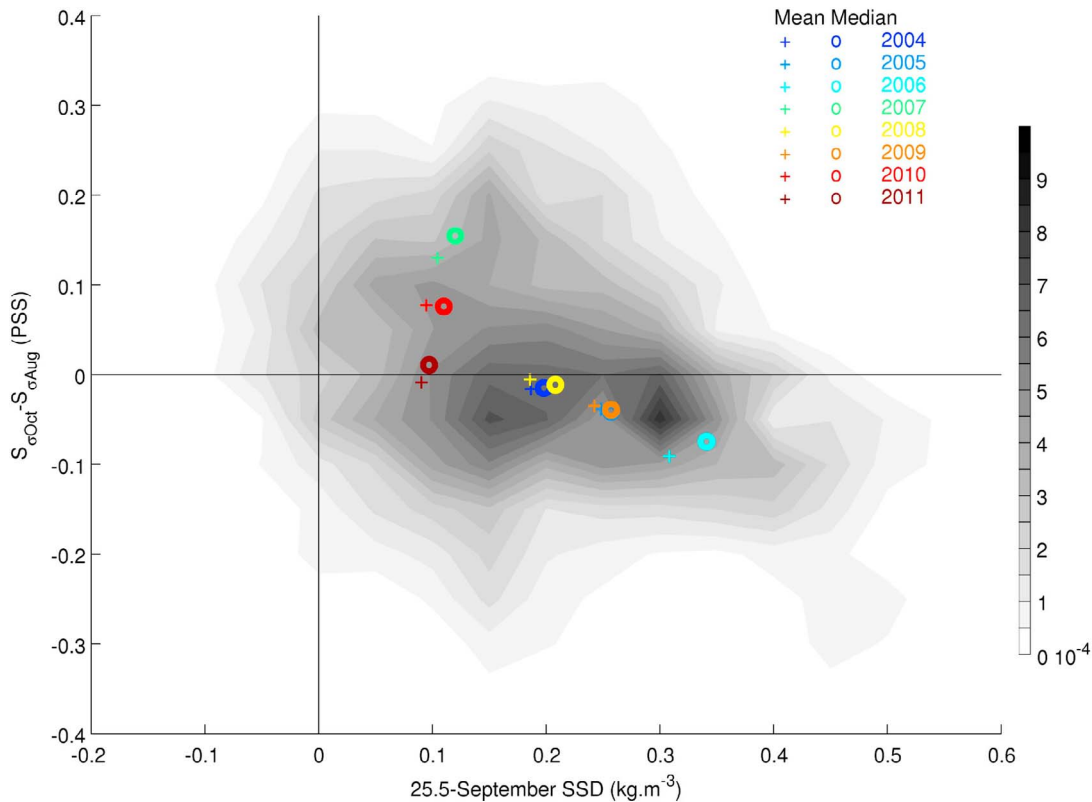


Figure 12. Density of grid point as a function of the difference between 25.5 kg.m^{-3} and the September Sea Surface Density, and the late winter anomaly injection, defined as the difference between October and August interannual salinity anomalies on $\sigma_\theta = 25.5$. Only the grid points within the source regions (>0.12 PSS in Figure 9) are included. The crosses and circles indicate the mean and median position, respectively, for the grid points corresponding to each individual year between 2004 and 2011.

[37] In numerical models, density-compensated anomalies in the SEP are injected by vertical mixing at the base of the mixed layer together with the destabilizing effect of the vertical gradient of salinity [Yeager and Large, 2004; Luo et al., 2005]. The Turner angle is a measure of density compensation, it can be used to characterize areas of spiciness formation. Yeager and Large [2007] evidenced the existence of injection mechanisms with Argo data in the SEP through an examination of the bulk Turner angle within the 200 shallowest meters depth, but could not observe the interannual variability of such a process. A similar computation is done here in the ARIVO fields, over the 2004–2011 period, using the definition provided by Yeager and Large [2007]:

$$Tu_b = \text{atan}\left(\frac{\alpha\Delta_{200}T + \beta\Delta_{200}S}{\alpha\Delta_{200}T - \beta\Delta_{200}S}\right) \quad (3)$$

where Δ_{200} is the difference between surface and 200 m depth value of the parameter, α and β the thermal expansion and haline contraction coefficient of the seawater, respectively.

[38] The high values of bulk Turner angles ($Tu_b > 70^\circ$ in Figure 13) are located in the southeastern sector of the maximum SSS (see Figure 9) in the density-compensated formation zones of the SEP. The maximum-SSS regions play a key role in the spiciness formation since they are area of strong destabilizing vertical salinity gradient [Blanke et al., 2002; Luo et al., 2005; Yeager and Large, 2004, 2007].

The highest bulk Turner angle values occur at the end of austral winter (September) in the region located between 32°S and 15°S , north of the late winter outcrop position. They are strongest during late winters 2007, 2010. This is consistent with the intense generation of spiciness anomalies during these years.

[39] To investigate the interannual variability of spiciness injection in the SEP as well as its vertical penetration, the Turner angle computed at the base of the mixed layer in the $35\text{--}15^\circ\text{S}/130\text{--}80^\circ\text{W}$ box (equation (2) and Figure 14) was quantified as a function of its distribution on selected isopycnal layers. During the early stage of the austral winter the values of Turner angles proved to be low and associated with few samples; at the end of the austral winter we observe the highest values of Turner angles (not shown). Figure 14 shows the distribution of the high values of Turner angle ($>71^\circ$) by density classes during the month of September. The isopycnal layer mainly affected by vertical mixing and spiciness injection lies within the $\sigma_\theta = 24.5$ and $\sigma_\theta = 25.8$ surfaces.

[40] The highest values of Turner angle are the most numerous in 2007, 2010 and 2011 in the isopycnal layer within $\sigma_\theta = 25.3$ and $\sigma_\theta = 25.8$ (and to a lesser extend in 2004). This suggests that vertical mixing and spiciness injection are greater at these isopycnal levels. The mechanisms at play in spiciness generation by vertical mixing at the base of the mixed layer [Yeager and Large, 2004, 2007] are consistent with the spiciness anomalies observed with the

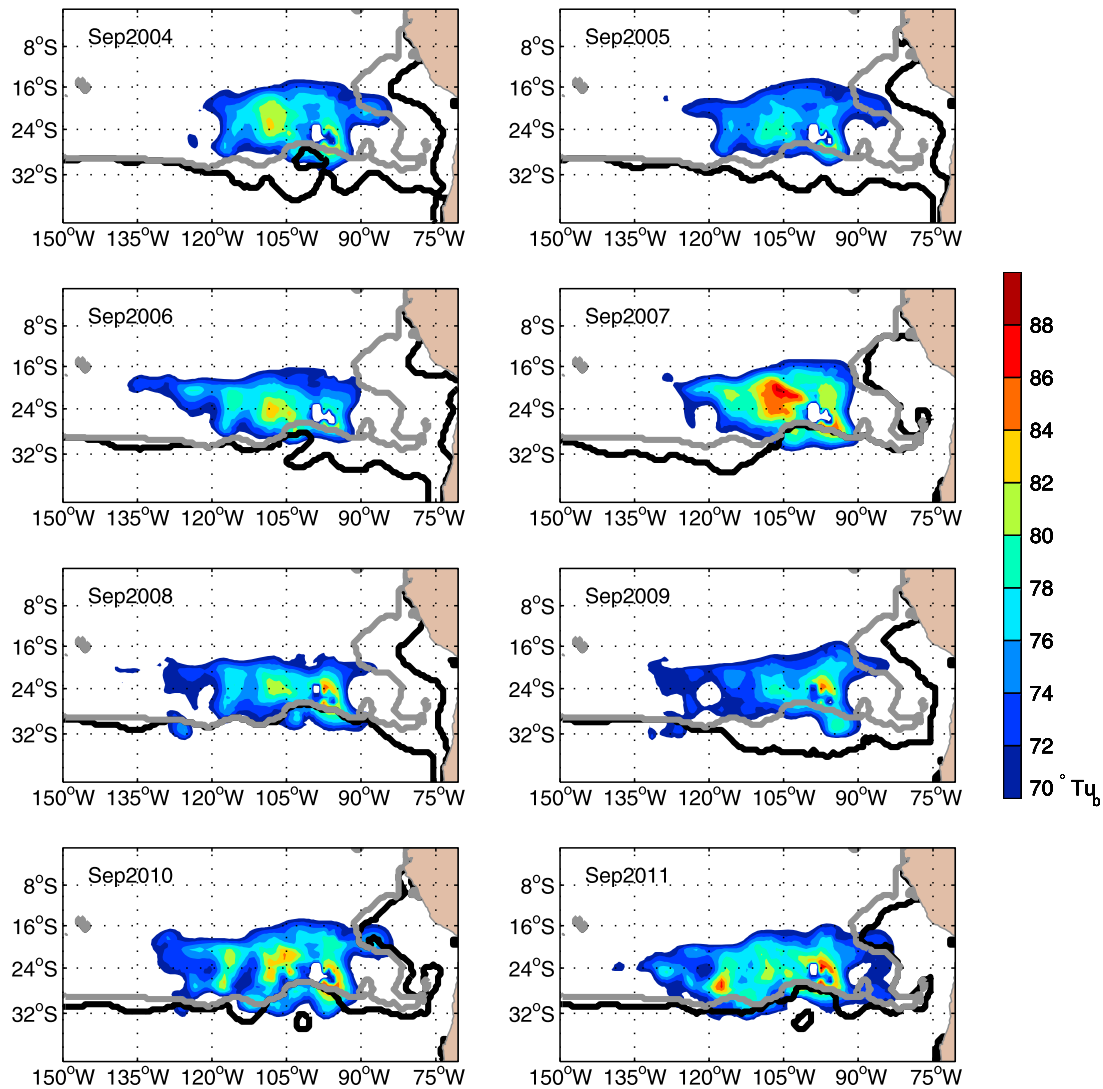


Figure 13. Bulk Turner angles between 0 and 200 m depth (Tu_b) computed in the September month for each year between 2004 and 2011 in the SEP. As in Figure 10, the thick gray line indicates the most equatorward outcrop position between 2004 and 2011. The thick black line indicates the September outcrop position during corresponding years indicated in each sub-figure.

present data set. It is also worth noting that in 2005 and 2009, for instance, a lighter $\sigma_\theta = 24.5\text{--}25.3$ isopycnal layer is affected by less spiciness injection; suggesting a shallower penetrative mixed layer during these austral winters, which leads to less spiciness injection in lighter waters. In contrast, the deeper penetration of the mixed layer (greater surface loss of buoyancy) that occurs in 2007, 2010 and 2011 is clearly associated with the intensified generation of spiciness positive anomalies on the $\sigma_\theta = 25.5$.

4.2. Sensitivity to the Mixed Layer Depth

[41] In order to link the anomalous deepening of the mixed layer in the SEP during the austral winter with the basin scale variability, a C-EOF analysis was made on the mixed layer depth interannual anomaly in the Pacific basin between 35°S-N (Figure 15). The STD associated with the first C-EOF mode (20.3% of explained variance; Figure 15a)

shows larger interannual anomalies in the Southern Hemisphere, and in particular in the SEP, associated with an amplitude greater than 16 m. The imaginary part (Figure 15c) of the first C-EOF mode displays a maximum of variance in the Southern Hemisphere, while the real part variance (Figure 15b) is higher in the tropical western Pacific west of 160°W with two branches extending east of 150°W to 30°N and 20°S ; both are 180° out of phase with the variance in the eastern equatorial Pacific. Particularly in the SEP, high mixed layer depth variance is collocated with region of maximum SSS (Figure 15c). The principal components of both real and imaginary parts are significantly correlated with the ENSO index (Figure 15c; gray; [$c_{\text{real}} = 0.87$; $\text{lag}_{\text{real}} = -1$ month; $c_{95\%} = 0.74$] and [$c_{\text{imag}} = 0.67$; $\text{lag}_{\text{imag}} = -6$ months; $c_{95\%} = 0.12$]). The variability of mixed layer in the SEP is closely correlated with the ENSO index. In particular, the mixed layer depth is the deepest during the austral winters following the El-Niño

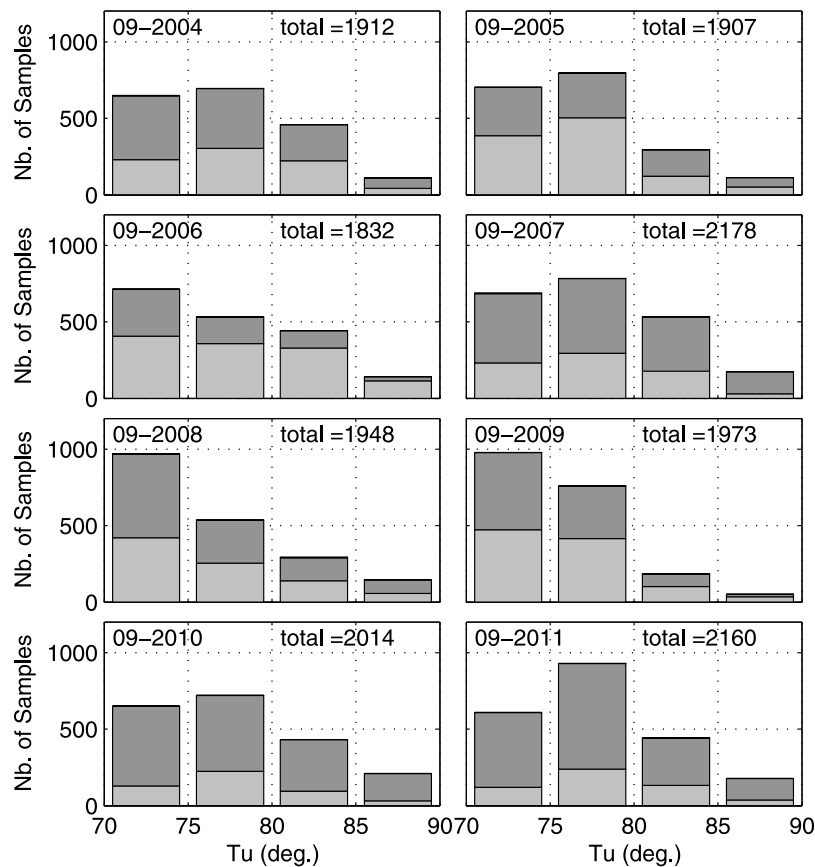


Figure 14. Distribution of Turner angles computed at the base of the mixed layer in the SEP box chosen between 130°W – 80°W and 35°S – 15°S for each T-S profile of ARIVO product versus both their value between 70° and 90° and of selected classes of water mass (named $\sigma_{\theta} = 24.5$ – 25.3 in light gray and 25.3 – 25.8 in dark gray) during the month of September of each year from 2004 to 2011.

events of 2006–2007 and 2009–2010 (Figure 15d). These observations suggest a link between ENSO variability and the mixed layer depth in the SEP.

[42] According to the ARIVO analysis, the most intense density compensated salinity anomaly generation is observed on $\sigma_{\theta} = 25.5$ (Figure 14) over the austral winters of 2007 and 2010 that follow the peaks of El-Niño in the tropical Pacific. These observations are in favor of a potential control of spiciness injection in the remote subtropical region of the SEP by atmospheric interannual variability. The remote connection and coupling between equatorial ENSO variability and subtropical subduction need to be addressed to better understand the interannual and decadal variability and its potential coupling with a spiciness mode [Schneider, 2000] in the southern Pacific Ocean.

[43] In conclusion, a stronger winter cooling produces a more equatorward excursion of the outcropping of density surfaces and deeper mixed layer due to a greater surface buoyancy loss. It allows a greater convection at the base of the mixed layer because of the destabilizing effect of the vertical gradient of salinity, which positively feeds back the deepening of the mixed layer. Subsequently, a larger amount of density compensated water masses are injected in the interior density layers that do not outcrop when the late winter mixed layer is deepest in the SEP. Therefore, the mixed layer depth could also

be an indicator associated with spiciness generation in the SEP [Yeager and Large, 2004, 2007].

5. Summary and Discussion

[44] The unprecedented data set provided by the Argo float measurements is used to observe the interannual variability of spiciness in the Pacific pycnocline between 2004 and 2011. During this 8 years period, spiciness anomalies appear in the northeastern and southeastern Pacific and propagate toward the western tropics. They are mainly advected by the mean currents within the pycnocline in both hemispheres, but their amplitude strongly decreases along the way. In the Northern Hemisphere, three strong anomalies (2 negative and 1 positive) were observed on $\sigma_{\theta} = 25.5$. In the Southern Hemisphere, four anomalies were generated in the SEP (2 positive and 2 negative). This result corroborates the previous numerical model and recent observational studies [e.g. Schneider *et al.*, 1999; Yeager and Large, 2004; Luo *et al.*, 2005; Nonaka and Sasaki, 2007; Sasaki *et al.*, 2010; Ren and Riser, 2010].

[45] The negative spiciness anomaly propagating in the Northern Hemisphere between 2004 and 2010 (Figure 6a) has been already observed by Sasaki *et al.* [2010], but the present study provides the first documented evidence of two more anomalies in this hemisphere: a positive spiciness

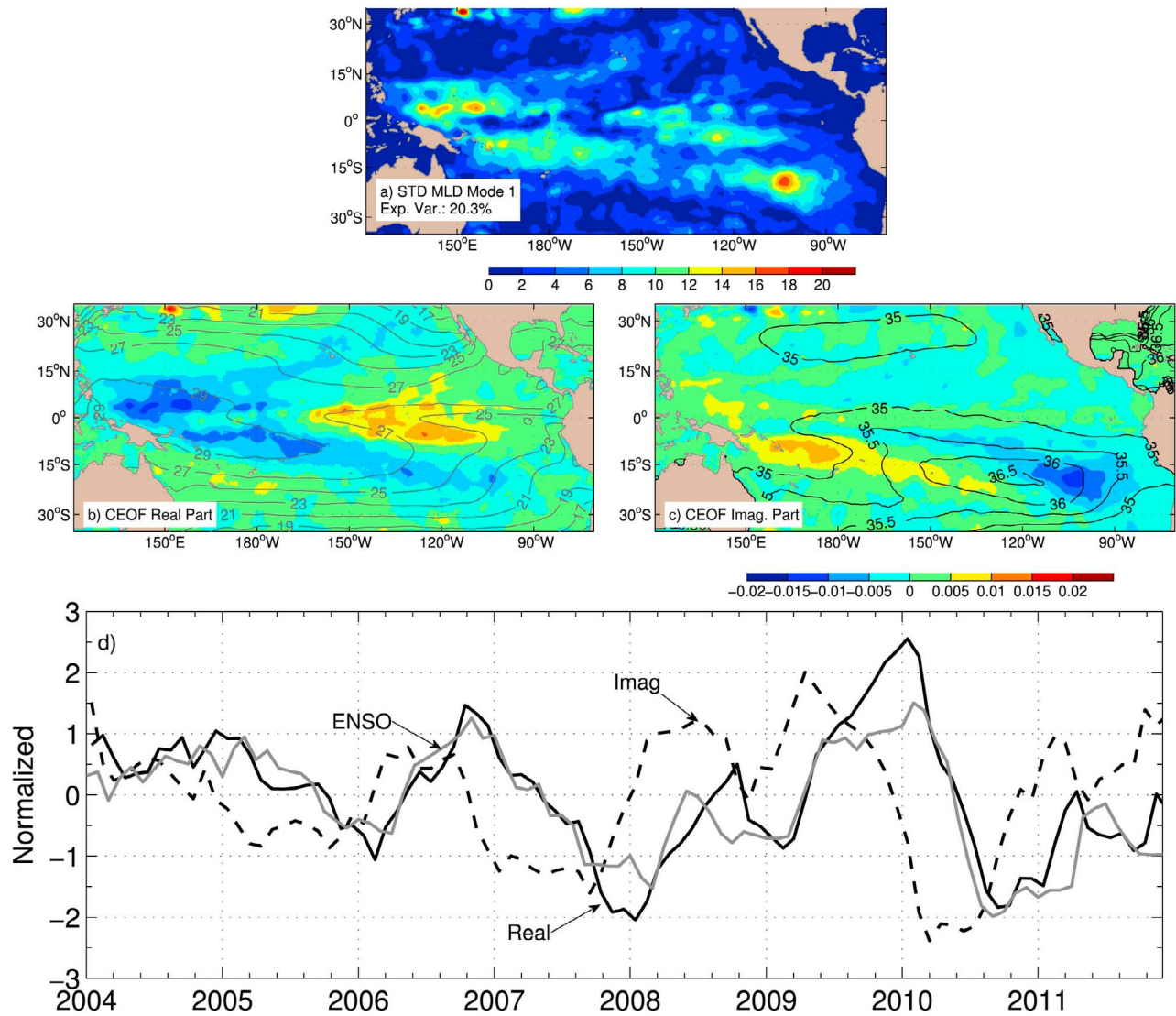


Figure 15. (a) Standard deviation, (b) real and (c) imaginary patterns of the first C-EOF mode performed on the mixed layer depth interannual anomaly over the Pacific Ocean between 35°S - 35°N , and (d) the associated time series of the principal components of the real (black solid) and imaginary (black dashed) parts. Plot of ENSO index for comparison with the time series of the C-EOF principal components (solid gray curve). Contour lines of the mean winter SST (Figure 15b) and SSS (Figure 15c) in the Northern (JFM) and Southern (JAS) Hemisphere.

anomaly from 2005 to 2011 and a negative spiciness anomaly generated in 2007. Such spiciness anomalies seem to emanate north of 35°N with a generation time-scale of about 5–7 years, and then grow in subsurface to reach maximum amplitude around 25 – 35°N . The generation of spiciness within the pycnocline in the NEP, was not clearly linked with SST and SSS neither with subsurface injection (not shown). The stochastic atmospheric forcing of the surface ocean at midlatitude may also contribute to the generation of spiciness anomalies in the NEP [Hasselmann, 1976; Kilpatrick *et al.*, 2011]. Thus, the spiciness generation mechanism in the NEP region is not fully resolved, even though the PDO variability is suspected to play a key role in the control of the decadal time-scale of winter generation of spiciness. It would be worth carrying out further studies based on longer time series as could be done in numerical models.

[46] This study addressed for the first time the interannual variability of intrapycnocline spiciness anomaly in the Southern Hemisphere. The variability of the spiciness signal on the $\sigma_{\theta} = 25.5$ is found to be higher in the SEP than in the NEP, and significantly correlated with ENSO variability. In the eastern basin between 32°S – 15°S , the bulk of density-compensated anomalies is clearly generated in the interior pycnocline during the austral winter on $\sigma_{\theta} = 25.5$ through enhanced vertical mixing at the base of the mixed layer because of destabilizing effect of vertical salinity profiles [Yeager and Large, 2004, 2007]. On interannual time scales, the late winter subduction process [Nonaka and Sasaki, 2007] appears to contribute weakly to the generation of positive spiciness anomaly, even though a link was clearly observed with our data between the equatorward position of the $\sigma_{\theta} = 25.5$ outcrop line and spiciness anomalies

generation. The injection of spiciness anomalies in this region proved to be significantly correlated with ENSO index. Their occurrence over the austral winter following an El-Niño event suggests an impact of the tropical variability on the subtropical spiciness generation in the SEP. The surface northward anomalous meridional migration of outcrop lines over the year following an El-Niño event and its phase-locking with the austral winter season [Jin and Kirtman, 2010] is clearly associated with enhanced injection of spiciness within the thermocline. In contrast, Kessler [1999] using cruises CTD data collected between 1984 and 1997, could not find an obvious relation between the surface hydrological variability in the SEP and the large tongue of high salinity on $\sigma_\theta = 24.5$ in the southern tropical Pacific. During the austral winter, the $\sigma_\theta = 24.5$ migrates northward beyond both the maximum SSS zone and the high Turner angle area (not shown), which is out of the spiciness generation zone. It is worth wondering whether the variability of the high-salinity tongue observed by Kessler [1999] on $\sigma_\theta = 24.5$ is subducted in the SEP, or rather associated with equatorial adjustment of the water masses in the upper thermocline [Kessler, 1999; Capotondi et al., 2005], or variability of the South Equatorial Current (SEC) associated with El-Niño variability [Kessler, 1999].

[47] The lack of match between the first mode of C-EOF in the Southern Hemisphere and the mean velocity field, in particular in the western Tropical Pacific north of 15°S is in favor of other mechanisms than spiciness propagation in the tropical western Pacific. For example, previous studies [Capotondi et al., 2005; Clarke et al., 2007; Clarke, 2010] have highlighted the role of baroclinic adjustment of the equatorward pycnocline transport, which results from westward traveling equatorial Rossby waves. Coupled model experiment and observations have also shown the role of wind curl in the southwestern Tropical Pacific liable to force decadal anomalies of meridional transport toward the western equatorial Pacific pycnocline [Luo et al., 2005; Cibot et al., 2005; Choi et al., 2009; Doney et al., 2007].

[48] The attenuation of spiciness anomalies along their travel remains to be explained. As shown by Sasaki et al. [2010], the overshoot of spiciness anomaly in the shadow zone of the northeastern Pacific between 5 and 15°N, is also suggested by our study, and probably operates in the Southern Hemisphere tropical shadow zone, which could lead to the attenuation of the spiciness on its main path. Moreover, the dispersion of tracer and/or vertical double-diffusivity [Johnson, 2006; Sato and Suga, 2009] and horizontal eddy mixing could erode the spiciness signature along their path [Fukumori et al., 2004; Sasaki et al., 2010]. Finally, the fate of spiciness reaching the boundary currents remain unknown. From a high-resolution numerical-simulation of Salomon Sea pathway of western boundary currents, Melet et al. [2011] demonstrated that water masses leaving the north Vitiaz straight for the equatorial currents are suspected to lose their spiciness signature because of intense horizontal mixing during their travel across the Salomon Sea. Sustained Argo observations in the near future should provide a remarkable tool to investigate these issues on a time-scale longer than the interannual one.

[49] Though we observed the arrival of a weak fresh anomaly into the western tropics potentially liable to impact the freshwater and heat budget of the equatorial thermocline, the lack of longer time series prevented us from observing

the impact of interannual anomalies generated after 2007 and from testing the hypothesis of a Southern Hemisphere subtropical ENSO weak feedback [Schneider, 2004]. For the moment, inferring such a spiciness mode in the Pacific ocean [Gu and Philander, 1997; Schneider, 2004; Liu and Alexander, 2007] as well as the potential link between the decadal spiciness variability with long-term ENSO modulation [Deser et al., 2004; Schneider, 2004; Choi et al., 2009] is still difficult. The potential source of extra-equatorial spiciness for the fresh water and heat of the equatorial upwelling [Fukumori et al., 2004] is however suggested by our data. For the moment, the present observations confirm the numerical results obtained by Schneider [2004]: only very weak interannual spiciness anomalies reach the tropical Pacific, which seriously compromises a significant impacts on the equatorial heat and freshwater budget as well such a spiciness mode in the Southern Hemisphere.

[50] In conclusion, this study demonstrated the benefits offered by the Argo data set for the monitoring of monthly to interannual variability (8 years, here) of complete subsurface hydrological structure of the upper 2 000 m depth of the Pacific Ocean. In the near future, the sustained Argo array of profiling floats would provide a remarkable tool to infer the decadal variability in the whole Pacific thermocline and a potential spiciness mode at this time scale.

[51] **Acknowledgments.** This work was funded by Ifremer project ‘Ocean and climate-SO-Argo’ and by CNES-TOSCA project ‘GLOSCAL’. N. Kolodziejczyk was supported by an Ifremer post-doctoral grant. The altimeter fields were produced by Ssalto/Duacs and distributed by Aviso with support from Cnes (<http://www.aviso.oceanobs.com/duacs/>). MDT_CNES-CLS09 was produced by CLS Space Oceanography Division and distributed by Aviso with support from Cnes (<http://www.aviso.oceanobs.com/>). The authors would like to thank Gilles Reverdin for useful comments on the manuscript. The authors thank anonymous reviewers for their remarks and corrections that helped to substantially improve the manuscript.

References

- Antonov, J., R. Locarnini, T. Boyer, A. Mishonov, and H. Garcia (2006), *World Ocean Atlas 2005*, vol. 2, *Salinity*, NOAA Atlas NESDIS, vol. 62, edited by S. Levitus, 182 pp., NOAA, Silver Spring, Md.
- Barnett, T. P. (1983), Interaction of the monsoon and Pacific trade wind systems at interannual time scales, Part I: The equatorial zone, *Mon. Weather Rev.*, *111*, 756–773, doi:10.1175/1520-0493(1983)111<0756:IOTMAP>2.0.CO;2.
- Blanke, B., M. Arhan, A. Lazar, and G. Prévost (2002), A Lagrangian numerical investigation of the origins and fates of the salinity maximum water in Atlantic, *J. Geophys. Res.*, *107*(C10), 3163, doi:10.1029/2002JC001318.
- Capotondi, A., M. A. Alexander, C. Deser, and M. J. McPhaden (2005), Anatomy and decadal evolution of the Pacific Subtropical-Tropical Cells (STCs), *J. Clim.*, *18*, 3739–3758.
- Choi, J., An S.-I., B. Dewitte, and W. W. Hsieh (2009), Interactive feedback between the tropical Pacific decadal oscillation and ENSO in the coupled general circulation model, *J. Clim.*, *22*, 6597–6610.
- Cibot, C., E. Maisonnavé, L. Terray, and B. Dewitte (2005), Mechanisms of tropical Pacific interannual-to-decadal variability in the ARPEGE/ORCA global coupled model, *Clim. Dyn.*, *24*, 823–842, doi:10.1007/s00382-004-0513-y.
- Clarke, A. J. (2010), Analytical theory for the quasi-steady and low-frequency equatorial ocean response to wind forcing: The “tilt” and “warm water volume” modes, *J. Phys. Oceanogr.*, *40*, 121–137, doi:10.1175/2009JPO4263.1.
- Clarke, A. J., S. Van Gorder, and G. Colantuono (2007), Wind stress curl and ENSO discharge/resharge in the equatorial Pacific, *J. Phys. Oceanogr.*, *37*, 1077–1091.
- Deser, C., A. S. Philips, and J. W. Hurrell (2004), Pacific interdecadal climate variability: Linkage between tropics and the North Pacific during boreal winter since 1900, *J. Clim.*, *17*, 3109–3124.
- Doney, S. C., S. Yeager, G. Danabasoglu, W. G. Large, and J. C. McWilliams (2007), Mechanisms governing interannual variability of the upper-ocean

- temperature in a global ocean hindcast simulation, *J. Phys. Oceanogr.*, *37*, 1918–1938, doi:10.1175/JPO3089.1.
- Ducet, N., P.-Y. Le Traon, and G. Reverdin (2000), Global high resolution mapping of ocean circulation from Topex/Poseidon and ERS-1 and -2, *J. Geophys. Res.*, *105*(C8), 19,477–19,498, doi:10.1029/2000JC900063.
- Fukumori, I., T. Lee, B. Cheng, and D. Menemenlis (2004), The origin, pathway, and destination of Niño-3 water estimated by a simulated passive tracer and its adjoint, *J. Phys. Oceanogr.*, *34*, 582–604, doi:10.1175/2515.1.
- Gaillard, F., E. Autret, V. Thierry, P. Galaup, C. Coatanoan, and T. Loubrieu (2009), Quality control of large Argo datasets, *J. Atmos. Oceanic Technol.*, *26*, 337–351, doi:10.1175/2008JTECHO552.1.
- Gu, D., and S. G. H. Philander (1997), Interdecadal climate fluctuation that depend on exchanges between the tropics and extratropics, *Science*, *275*, 805–807, doi:10.1126/science.275.5301.805.
- Hasselmann, K. (1976), Stochastic climate models. Part 1, Theory, *Tellus*, *28*, 473–485, doi:10.1111/j.2153-3490.1976.tb00696.x.
- Jin, D., and B. P. Kirtman (2010), How the annual cycle affects the extratropical responses to ENSO, *J. Geophys. Res.*, *115*, D06102, doi:10.1029/2009JD012660.
- Johnson, G. C. (2006), Generation and initial evolution of a mode water θ -S anomaly, *J. Phys. Oceanogr.*, *36*, 739–751, doi:10.1175/JPO2895.1.
- Johnson, G. C., and M. J. McPhaden (1999), Interior pycnocline flow from the subtropical to the equatorial Pacific Ocean, *J. Phys. Oceanogr.*, *29*, 3073–3089, doi:10.1175/1520-0485(1999)029<3073:IPFFTS>2.0.CO;2.
- Kessler, W. S. (1999), Interannual variability of the subsurface high salinity tongue south of the equator at 165°E, *J. Phys. Oceanogr.*, *29*, 2038–2049.
- Kilpatrick, T., N. Schneider, and E. Di Lorenzo (2011), Generation of low-frequency spiciness variability in the thermocline, *J. Phys. Oceanogr.*, *41*, 365–377, doi:10.1175/2010JPO4443.1.
- Laurian, A., A. Lazar, G. Reverdin, K. Rodgers, and P. Terray (2006), Poleward propagation of spiciness anomalies in the North Atlantic Ocean, *Geophys. Res. Lett.*, *33*, L13603, doi:10.1029/2006GL026155.
- Laurian, A., A. Lazar, and G. Reverdin (2009), Generation mechanism of spiciness anomalies: An OGCM analysis in the North Atlantic subtropical gyre, *J. Phys. Oceanogr.*, *39*, 1003–1018, doi:10.1175/2008JPO3896.1.
- Lazar, A., R. Murtugudde, and A. J. Busalacchi (2001), A model study of temperature anomaly propagation from subtropics to tropics within the South Atlantic thermocline, *Geophys. Res. Lett.*, *28*, 1271–1274.
- Lazar, A., T. Inui, P. Malanotte-Rizzoli, A. J. Busalacchi, L. Wang, and R. Murtugudde (2002), Seasonality of the ventilation of the tropical Atlantic thermocline in an ocean circulation model, *J. Geophys. Res.*, *107*(C8), 3104, doi:10.1029/2000JC000667.
- Liu, Z. (1994), A simple model of mass exchange between the subtropical and tropical ocean, *J. Phys. Oceanogr.*, *24*, 1153–1165.
- Liu, Z. (1999), Forced planetary wave response in a thermocline gyre, *J. Phys. Oceanogr.*, *29*, 1036–1055.
- Liu, Z., and M. Alexander (2007), Atmospheric bridge, oceanic tunnel, and global climatic teleconnections, *Rev. Geophys.*, *45*, RG2005, doi:10.1029/2005RG000172.
- Liu, Z., and S.-I. Shin (1999), On the thermocline ventilation of active and passive tracers, *Geophys. Res. Lett.*, *26*, 357–360, doi:10.1029/1998GL900315.
- Locarnini, R., A. Mishonov, J. Antonov, T. Boyer, and H. Garcia (2006), *World Ocean Atlas 2005*, vol. 1, *Temperature*, NOAA Atlas NESDIS, vol. 61, edited by S. Levitus, 182 pp., NOAA, Silver Spring, Md.
- Luo, J.-J., and T. Yamagata (2001), Long-term El Niño-Southern Oscillation (ENSO)-like variation with special emphasis on the South Pacific, *J. Geophys. Res.*, *106*, 22,211–22,227.
- Luo, Y., L. M. Rothstein, R.-H. Zhang, and A. J. Busalacchi (2005), On the connection between South Pacific subtropical spiciness anomalies and decadal equatorial variability in an ocean general circulation model, *J. Geophys. Res.*, *110*, C10002, doi:10.1029/2004JC002655.
- Luyten, J. R., J. Pedlosky, and H. Stommel (1983), The ventilated thermocline, *J. Phys. Oceanogr.*, *13*, 292–309, doi:10.1175/1520-0485(1983)013<0292:TVT>2.0.CO;2.
- Maximenko, N., P. Niiler, M.-H. Rio, O. Melnichenko, L. Centurioni, D. Chambers, V. Zlotnicki, and B. Galperin (2009), Mean dynamic topography of the ocean derived from satellite and drifting buoy data using three different techniques, *J. Atmos. Oceanic Technol.*, *26*, 1910–1919, doi:10.1175/2009JTECHO672.1.
- McDougall, T. J., and A. Klocker (2010), An approximate geostrophic streamfunction for use in density surface, *Ocean Modell.*, *32*, 105–117, doi:10.1016/j.ocemod.2009.10.006.
- Melet, A., J. Verron, L. Gourdeau, and A. Koch-Larrouy (2011), Equatorward Pathways of Salomon Sea Water Masses and Their Modification, *J. Phys. Oceanogr.*, *41*, 810–826, doi:10.1175/2010JPO4559.1.
- Nonaka, M., and H. Sasaki (2007), Formation Mechanism for Isopycnal Temperature-Salinity Anomalies Propagating from the Eastern South Pacific to the Equatorial Region, *J. Clim.*, *20*, 1305–1315, doi:10.1175/JCLI4065.1.
- Ren, L., and S. C. Riser (2010), Observations of decadal time scale salinity change in the subtropical thermocline of the North Pacific Ocean, *Deep Sea Res. II*, *57*, 1161–1170.
- Rio, M.-H., S. Guinehut, and G. Larnicol (2011), The New CNES-CLS09 global mean dynamic topography computed from the combination of GRACE data, altimetry and in-situ measurement, *J. Geophys. Res.*, *116*, C07018, doi:10.1029/2010JC006505.
- Ruddick, B. (1983), A practical indicator of stability of the water column to double-diffusive activity, *Deep Sea Res. A*, *30*, 1105–1107.
- Sasaki, Y. N., N. Schneider, N. Maximenko, and K. Lebedev (2010), Observational evidence for propagation of decadal spiciness anomalies in the North Pacific, *Geophys. Res. Lett.*, *37*, L07708, doi:10.1029/2010GL042716.
- Sato, K., and T. Suga (2009), Structure and modification of the South Pacific Eastern Subtropical Mode Water, *J. Phys. Oceanogr.*, *39*, 1700–1714, doi:10.1175/2008JPO3940.1.
- Schneider, N. (2000), A decadal spiciness mode in the tropics, *Geophys. Res. Lett.*, *27*, 257–260, doi:10.1029/1999GL002348.
- Schneider, N. (2004), The response of the tropical climate to the equatorial emergence of spiciness anomaly, *J. Clim.*, *17*, 1083–1095, doi:10.1175/1520-0442(2004)017<1083:TROTCT>2.0.CO;2.
- Schneider, N., A. J. Miller, M. A. Alexander, and C. Deser (1999), Subduction of decadal North Pacific temperature anomalies: observations and dynamics, *J. Phys. Oceanogr.*, *29*, 1056–1070.
- Tailleux, R., A. Lazar, and C. J. C. Reason (2005), Physical and dynamics of density-compensated temperature and salinity anomalies. Part I: Theory, *J. Phys. Oceanogr.*, *35*, 849–864, doi:10.1175/JPO2706.1.
- von Schuckmann, K., F. Gaillard, and P.-Y. Le Traon (2009), Global hydrographic variability patterns during 2003–2008, *J. Geophys. Res.*, *114*, C09007, doi:10.1029/2008JC005237.
- Yeager, G. S., and W. G. Large (2004), Late-winter generation of spiciness on subducted isopycnals, *J. Phys. Oceanogr.*, *34*, 1528–1547, doi:10.1175/1520-0485(2004)034<1528:LGOSOS>2.0.CO;2.
- Yeager, G. S., and W. G. Large (2007), Observational evidence of winter spice injection, *J. Phys. Oceanogr.*, *37*, 2895–2919, doi:10.1175/2007JPO3629.1.
- You, Y. (2002), A global ocean climatological atlas of the Turner angle: Implications for the double-diffusion and water-mass structure, *Deep Sea Res., Part I*, *49*, 2075–2093, doi:10.1016/S0967-0637(02)00099-7.
- Zhang, R.-H., and Z. Liu (1999), Decadal thermocline variability in the North Pacific Ocean: Two pathways around the subtropical gyre, *J. Phys. Oceanogr.*, *29*, 3273–3296.